EFFICIENT ANALYSIS OF GENERAL CREEPING MOTION OF A SPHERE INSIDE A CYLINDER

by

COLUMBIA MISHRA, B.M.E.

A THESIS

IN

MECHANICAL ENGINEERING

Submitted to the Graduate Faculty
of Texas Tech University in
Partial Fulfillment of
the Requirements for
the Degree of

MASTER OF SCIENCE

IN

MECHANICAL ENGINEERING

Approved

Sukalyan Bhattacharya

Chairperson of the Committee

Rajesh Khare

Michelle L. Pantoya

Accepted

Fred Hartmeister

Dean of the Graduate School

May, 2008

ACKNOWLEDGEMENTS

I want to thank my family for being such a huge support all throughout my Master's. Without their love and support, these past two years would have been much more trying. I would like to thank Dr. Sukalyan Bhattacharya who provided the right combination of guidance and free reign to allow me to learn and develop both as a researcher and an individual. I have enjoyed working with you. Thank you for all your support and for being such a wonderful teacher. I am thankful to Dr. Rajesh Khare and Dr. Michelle L. Pantoya for being there in my thesis committee. Thanks to Sonal for being such a great friend to me all this time. I want to thank Dr. Delong Zuo from Wind Science and Engineering Research Center and M. Vignarajah from the Department of Civil Engineering for supporting me and helping me with my thesis formatting. Thanks to Dr. Darryl James and Dr. Alexander Idesman for helping me with LaTex. I would like to acknowledge my lab-mates Dil, Shahin, Richard, Martin and Shivesh who made it an interesting time in the lab and in the school. Thanks to all my friends in Lubbock who made these two years enjoyable. I want to take the opportunity to tell my parents Jai Prakash and Minati that they are the best parents and without their encouragement I could not have come this far. I am lucky to have Chandragupta and Challenger as my brothers. Thank you for believing in me always. Finally, I would like to thank Texas Tech University and the Department of Mechanical Engineering for providing me with such a wonderful environment and learning experience for these two years.

CONTENTS

ABSTRACT

Creeping motion of a sphere in viscous fluid bounded by a cylindrical surface is crucial in many physical and physiological processes. In this thesis, I describe a very efficient method to comprehensively solve a classical flow problem involving suspended colloidal particles inside a conduit. A general solution technique is proposed to determine the hydrodynamic interactions between such spherical particles and cylindrical confinement.

In order to efficiently solve the Stokesian flow-field around a sphere inside a cylinder, we formulate a general mathematical procedure which can be used to find reflection relations for a vector field at simple surfaces. Unlike other recently developed efficient algorithms, the present technique does not require any translational symmetry. The method is based on the expansion of a vector field in terms of general separable basis functions. It enables us to solve a second order linear vector equation with specified conditions at disconnected bodies defined by planar, cylindrical and spherical boundaries. Thus, one can extend the outlined methodology to describe multiparticle hydrodynamic interactions in a cylinder or an annulus.

The main focus of this article is to provide a complete description of the dynamics of a spherical particle in a cylindrical vessel. For this purpose, we consider motion of the sphere in both quiescent fluid and pressure-driven parabolic flow. First, we determine the force and torque on a translating-rotating particle in quiescent fluid in terms of general friction coefficients. Then we assume an impending parabolic

flow and calculate the force and the torque on a fixed sphere as well as the linear and angular velocities of a freely moving particle. The results are presented for different radial positions of the particle and different ratios between the sphere and the cylinder radius. Because of the generality of the procedure, there is no restriction in relative dimensions, particle-position and direction of motion. For the limiting cases of geometric parameters, our results agree with the ones obtained by past researchers using different asymptotic methods.

LIST OF FIGURES

CHAPTER 1

INTRODUCTION

In this thesis I solve the hydrodynamic fields around a spherical particle in a cylindrical confinement. The flow under consideration is creeping motion and is one of the most widely prevalent flow systems in nature.

The simulated system represents transport of particulate complex-fluids through a cylinder. This type of flow is a very common phenomenon in biological or industrial systems which include blood-flow in blood-vessels of living organisms or flow of suspensions through micro-conduits in microfluidic devices. Further examples include settling of dust particles in fluid, fluid flow(oil or water) through small channels or cracks such as hydrodynamic lubrication or the seepage in sand or rock formations, swimming of micro-organisms, flow of lymphatic fluids inside the lymph duct, particles in the alveoli, particulate flow in sub-micron channels. Creeping flow of high viscosity fluid like extrusion of melts and the transport of paints and heavy oils are other industrial examples. Due to numerous technological applications, the hydrodynamic interaction between the particle and the walls of the bounded fluid is of immense importance.

These types of flow in microscopic domain have negligible inertia such that the Reynolds number, $Re = \rho l v/\mu << 1$. As a result we can simplify the analysis by creeping flow approximation where the non-linear inertia term is neglected in the governing Navier-Stokes equation. Accordingly the fluid mechanical equation can be

expressed by linear Stokesian equations.

We can find two sets of separable basis solutions for the resultant linearized Stokes equation. These basis solutions, thus obtained, are solved to satisfy the proper boundary conditions at both the spherical particle and the cylindrical conduit using required transformations and general reflection relations. The main focus of my thesis is this analysis and is discussed elaborately in the subsequent chapters.

1.1 Motivation from previous results and applications

The present study is a fundamental hydrodynamic analysis with vast applications in bioengineering. The reason for its importance in the bioengineering field is the system under consideration is a realistic model of complex body-fluids flowing in bio-conduits. The basic features of the biological system are similar to the simulated system; body-fluid like blood can be modeled as a multiparticle suspension with blood cells and macro-molecules [1, 2, 3] of varied geometry such as spherical or elliptical geometry, and bio-conduits like blood-vessels and capillaries can be approximated as cylindrical ducts. It is common in fluid-mechanical models to assume the suspended particles as spheres. Hence, for biological and microfluidic applications, it is necessary to analyze the hydrodynamic interactions between a spherical particle and a confining cylindrical surface.

The single particle and conduit system analysis considered here will be the basis for extension to multiparticle systems with suspended particles of complex geometries. Hence details from this research will be useful in the theoretical prediction of pressure loss in blood-vessels, rheological properties of confined body-fluids, flow-induced cell-

destruction and flow-induced conduit rupture. The research is also motivated from the emerging applications like micro-fluidic devices and production of photonic materials by self-assembly of colloidal crystals [4, 5].

A sound mathematical theory and an efficient simulation technique to describe many body interactions in cylindrical conduits are yet to be achieved in fluid-mechanical research. Recent experimental works in this field have produced new results using modern tools like microfluidic devices [6], sophisticated rheometers [7], microscopy equipments [8, 9, 10, 11, 12, 13], and flow instruments for clinical purposes [14, 15, 16, 17]. These modern technologies provide new insight into the role of interparticle hydrodynamic interactions in micron-size biofluidic systems. For example, recent haematological studies have shown that hydrodynamic stress-field on an individual cell plays a major role in the behavior of erythrocytes [1, 2, 3, 18, 19, 20], platelets [21, 22, 23, 24, 25, 26, 27, 28], neutrophils [29, 30, 31, 32, 33], and generic leukocytes [34, 35, 36, 37, 38, 39, 40]. Moreover, it has been seen that the detailed flow-pattern around a single cell affects substrate transport [41, 42], biocatalyst sensitivity [43], nitric oxide concentration [44] and ATP release [45]. This detailed knowledge is essential to address a wide range of clinical challenges [46] and cure diseases like sickle-cell blood defect [47, 48], metastasis tumor [49, 50, 51, 52], hypertension [53] and thalassemia [54].

The current continuum models are inadequate for this purpose. Hence it is required to have a new methodolgy which can accurately resolve particle-wall and particle-particle interactions. In theory, general techniques like boundary integral

method [55, 56, 57, 58, 59, 60, 61, 62] or molecular dynamics simulation [63, 64, 65, 66, 67, 68, 69, 70] can analyze creeping motion of arbitrary particles in arbitrary conduits. In practice, however, huge numerical cost restricts these general methods to systems with only a few particles. In contrast, for regular enough particle and conduit geometries, creeping motion of even a large number of particles can be described by fast algorithms based on basis solution expansion of Stokes equation. Such fast methods were used to solve Stokes flow around several spheres in unbounded [71, 72, 73] or planar wall bounded [74, 75, 76, 77, 78, 79] domains. However, a generalization of this technique to cylindrical conduits or ellipsoidal particles or non-Stokesian equations is still mathematically unapproachable.

My thesis concentrates on a single particle system but the methodology developed here is general enough to be extended to multi-particle systems. Hence it can be used as a model to solve complex multiparticle confined systems.

1.2 Related Work

In the past, several theoretical investigations have addressed classical flow-problems involving creeping motion of a sphere inside a cylinder. Earlier researchers predominantly focused on axial movement of the sphere. Their theories are primarily based on various approximate perturbative schemes which are only valid for different limiting cases [80]. These studies can be classified into three categories accordingly.

The first of these approximate techniques is referred as the method of reflection [81, 82, 83, 84, 85]. In this method, one initially finds the scattered flow from the sphere in free-space with no cylindrical confinement. A correction field is then subtracted to

nullify the non-zero velocity at the cylinder surface in the initial approximation. This ensures the satisfaction of the no-slip condition at the conduit, but creates an error in the boundary condition at the sphere surface. Hence, several similar iterations are subsequently performed for improvement which is only possible when the distance between the particle center and the cylinder is much larger than the sphere radius. Other equivalent regular perturbation schemes [86, 87] also have similar restriction.

When the distance between the particle-center and the conduit surface is comparable to the particle radius, the method of reflection can not be used. Then, in the limit of large ratio between the radii of the cylinder and the sphere, one can approximate the surface of the vessel to be nearly planar [88, 89, 90]. This second scheme, however, is not applicable when cylinder radius is comparable to the cylinder-sphere separation.

Finally, theoretical results are also available for configurations where the particle is very tightly fitted in the conduit [91, 92]. In such cases, one can use lubrication theory based on the singular perturbation technique to calculate the hydrodynamic friction or mobility of a sphere closely surrounded by a cylindrical surface.

Neither of these aforementioned analysis is, however, applicable when the sphere radius, the cylinder radius and the separation between surfaces of the sphere and the cylinder are comparable. This is why the existing theories are inadequate in describing various physically interesting phenomena (like cell dynamics in arterioles or microfluidic transports) where all three defining dimensions of the particle-conduit systems are of the same order. Also, the past studies were mainly focused on axial

motion of the particle. However, in presence of an external field like gravity acting in the cross-sectional plane of the cylinder, the particle can move in the radial and azimuthal directions also. To our knowledge, such complete description of the dynamics of the cylinder-sphere system is still not available. Hence, a more general formulation is required to understand particle-dynamics either in arbitrary geometry or under influence of arbitrary force fields.

The issue of generality can be addressed by several numerical techniques like boundary integral [93, 94], spectral boundary element [95], finite element [96, 97, 98] and molecular dynamics [99, 100] simulations. However, these well-known methods require a considerable computational cost. Thus, a more efficient algorithm is desirable to study colloidal systems in confinements especially if we want to extend the methodology to explain many-particle interactions.

In this paper, we present a semi-analytical procedure which can be efficiently implemented to solve general creeping flow problems involving spherical particles in cylindrical conduits. Our primary focus is to determine hydrodynamic interactions between a single spherical particle and one confining cylinder though the technique is general enough to be easily extended to multiparticle systems and annular geometries.

Our solution technique has similarities with Stokesian dynamics simulations (often referred as multipolar expansion) which utilize the solution of Stokes equation in spherical coordinates to solve multiparticle interactions in unbounded space [101, 102, 103, 104]. The method is extended to analyze colloidal systems in wall-bounded slit-pore by combining boundary integral and the spherical solutions [105]. The same

problem is also approximately solved by modeling the bounding planar walls as closely packed arrays of static spheres so that the free-space many-sphere computation can simply be extended without any further complexity [106, 107]. More accurate results can be obtained with even less cost, if the spherical solutions are applied in conjunction with proper reflection relations for a single planar wall [108, 109] or two such walls [110]. Recently, the efficiency has been further increased by devising a scheme which analyzes many-sphere problem between two planes by using two sets of Stokesian solutions (spherical and Cartesian) [77, 111, 79, 78]. Applicability of this efficient algorithm is, however, restricted to planar wall geometries due to its crucial dependence on translational symmetries which are not a necessity for the general formulation outlined in this paper.

1.3 Organization of present work

The presented method is based on the basis function expansion of a vector field governed by a second order linear differential equation. For our particular problem, the vector field is the flow field and the second order governing equation is the Stokes equation. Accordingly, we find the complete sets of separable basis solutions for the Stokes equation in cylindrical and spherical coordinates which correspond to the conduit and the particle surface, respectively. The separable solutions are used to find general reflection relations at the respective surfaces so that any prescribed field at the interfaces can be described appropriately. For simultaneous satisfaction of the boundary conditions at both spherical and cylindrical surfaces, proper transformation relations between spherical and cylindrical basis solutions are derived. These trans-

formation relations along with the reflection relations are used to obtain necessary results.

This paper is organized in the following manner. In chapter 2, we describe how we satisfy boundary conditions at disconnected simple surfaces by using separable basis solutions and general reflection relations. In chapter 3, we solve Stokes equation in the presence of a sphere inside a cylinder by following the outlined procedure. Numerical implementation and convergence tests are presented in chapter 4. In chapter 5, we apply our algorithm to find hydrodynamic friction coefficients of the particle translating and rotating in quiescent fluid for arbitrary geometric configurations and arbitrary direction of motion. In the limiting cases, we compare our results with existing data to validate our analysis. In chapter 6, we consider the particle to be in a pressure-driven parabolic flow, and determine the hydrodynamic friction when it is fixed as well as the hydrodynamic mobility when it is freely moving. Finally, the conclusions are drawn in chapter 7.

CHAPTER 2

BASIS TRANSFORMATION METHOD

In this chapter, we present an outline of the general mathematical procedure (referred as basis transformation method) that is used in our analysis. The key features of this method are similar to simple separation of variables used for solving a linear partial differential equation apart from two crucial differences. Firstly, in our problem the boundary conditions are specified at different kinds of disconnected surfaces (the conduit and the particle). Secondly, these conditions specify a vectorial field (velocity) instead of a scalar which is generally the dependent variable in the separation of variable.

2.1 Geometry and coordinate systems

In the analysis, we assign two different coordinate systems for the conduit and the particle assuming simple enough geometries for both. For a general particle and a general confinement these coordinates are denoted as (α, β, γ) and (α_1, β_1, γ_1), respectively. Accordingly, the conduit and the particle are described by α-constant and α_1-constant surfaces. For the particle-fluid interface, we consider $\alpha_1 = a_1$. If the confined domain is bounded by a single surface (as in one-wall or cylindrical geometries), we assume the surface is represented by $\alpha = a$. In contrast, if two isolated boundaries are present (as in two-wall or annular geometries), we define the

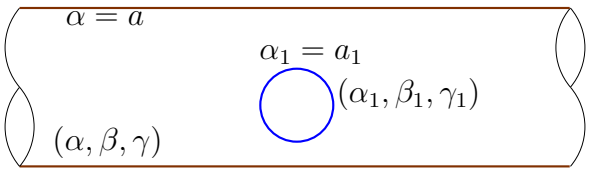

Figure 2.1: The conduit and the particle coordinates.

additional surface by $\alpha = a'$ with $a' < a$. Though our method can be applied for annular and two-wall geometries, at present, we only concentrate on a single-surface conduit which is the case for a cylindrical vessel.

Hence, in our specific problem, (α, β, γ) are cylindrical coordinates (ρ, β, z) with z axis coinciding with the conduit axis whereas (α_1, β_1, γ_1) are spherical coordinates (r, θ, ϕ) with origin at the particle center. So, according to our notation, the conduit radius is a and the particle radius is a_1. The specific geometry and coordinates are schematically described in Fig.2.1. It is to be noted that this general procedure also works for other geometries. For example, the conduit coordinates would be Cartesian if the confinement is a planar wall, or the particle coordinate will be spheroidal if the particle is a spheroid.

2.2 Complete set of separable basis solutions

Once the coordinates are assigned, we focus on the expression of general vectorially separable basis-solutions for the governing equation in both (α, β, γ) and (α_1, β_1, γ_1) coordinate systems. As the governing equation is second order, we need two independent solutions for each systems to properly solve the vector field. Accordingly, the separable basis solutions for the conduit and the particle coordinates are denoted as $\mathbf{v}^{\pm}_{\lambda\mu\sigma}$ and $\mathbf{v}^{1\pm}_{lm\sigma}$, respectively. The superscripts $+$ and $-$ represent two different kinds of solutions.

At this point, we provide a detailed description of the subscripts in $\mathbf{v}^{\pm}_{\lambda\mu\sigma}$ and $\mathbf{v}^{1\pm}_{lm\sigma}$ to clarify their meaning. The indices l and m are required to construct the complete set in scalar functional space for the particle coordinates. These are generally discrete numbers like the indices of spherical or spheroidal harmonics in spherical or spheroidal coordinates. On the other hand, λ and μ are indices associated to the scalar functional space in (α, β, γ) system. These indices can be either discrete or continuous depending on the confinements. For Stokesian fields near planar walls, λ

and μ are the x and y components of continuous wave-vectors whereas for cylindrical geometries λ is the magnitude of continuous wave-vector and μ is a discrete number associated with azimuthal dependence as $\exp(\mathrm{i}\mu\beta)$. The other index $\sigma = 0, 1, 2$ indicates three independent solutions which complete the set of vectorial basis functions in three dimensional space.

In order to satisfy arbitrary linear non-homogeneous boundary conditions at the particle and the conduit surface, $\mathbf{v}^{\pm}_{\lambda\mu\sigma}$ and $\mathbf{v}^{1\pm}_{lm\sigma}$ have to be in the following form:

$$\mathbf{v}^{\pm}_{\lambda\mu\sigma} = \mathbf{S} \cdot \sum_{s=0,1,2} \mathbf{e}_{\lambda\mu s}(\alpha, \beta, \gamma) f^{\pm}_{\lambda\mu s\sigma}(\alpha), \tag{2.1}$$

and

$$\mathbf{v}^{1\pm}_{lm\sigma} = \mathbf{S}^1 \cdot \sum_{s=0,1,2} \mathbf{e}^1_{lms}(\alpha_1, \beta_1, \gamma_1) \;\; f^{1\pm}_{lms\sigma}(\alpha_1). \tag{2.2}$$

The index-independent second order invertible tensorial functions $\mathbf{S}$ or $\mathbf{S}^1$ and index-dependent single-variable scalar functions $f^{\pm}_{\lambda\mu s\sigma}$'s or $f^{1\pm}_{lms\sigma}$'s in eqs.2.1 and 2.2 are to be determined for particular governing equations and coordinate systems. We also impose additional finiteness criteria so that for finite α and α_1 1) $f^{+}_{\lambda\mu s\sigma}$ is finite for $\alpha < \infty$, 2) $f^{-}_{\lambda\mu s\sigma}$ is finite for $\alpha > 0$, 3) $f^{1+}_{lms\sigma}$ is finite for $\alpha_1 < \infty$, 4) $f^{1-}_{lms\sigma}$ is finite for $\alpha_1 > 0$.

The vectors $\mathbf{e}_{\lambda\mu s}$ or $\mathbf{e}^1_{lms}$ form a complete set of orthogonal fields in terms of which any vector function can be expanded at α- or α_1-constant surface, respectively.

$$\int \mathbf{e}^{*}_{\lambda\mu s} \cdot \mathbf{e}_{\lambda'\mu's'} d\beta d\gamma = \delta_{\lambda\lambda'}\delta_{\mu\mu'}\delta_{ss'}, \tag{2.3}$$

and

$$\int \mathbf{e}^{1*}_{lms} \cdot \mathbf{e}^{1}_{l'm's'} d\beta_1 d\gamma_1 = \delta_{ll'}\delta_{mm'}\delta_{ss'}, \tag{2.4}$$

where the superscript $*$ denotes complex conjugate and δ is either the Kronecker delta

or the Dirac-delta function depending on whether the subscripts are discrete or not.

The presented method can be applied only when the governing equations and the geometries are such that the vector basis functions can be expressed by eqs.2.1 – 2.4. Fortunately, for common equations like steady or periodically transient Stokes equation and for simple geometries like spherical particles, cylindrical conduit or planar walls, such basis functions can be constructed. In all of these cases, the general solution for the vector field $\mathbf{v}$ can be expressed as a linear combination of either $\mathbf{v}^{\pm}_{\lambda\mu\sigma}$

$$\mathbf{v} = \sum\!\!\!\!\!\!\int_{\lambda\mu\sigma} (\mathbf{v}^{+}_{\lambda\mu\sigma} b^{+}_{\lambda\mu\sigma} + \mathbf{v}^{-}_{\lambda\mu\sigma} b^{-}_{\lambda\mu\sigma}), \tag{2.5}$$

or $\mathbf{v}^{1\pm}_{lm\sigma}$

$$\mathbf{v} = \sum_{lm\sigma} (\mathbf{v}^{1+}_{lm\sigma} c^{+}_{lm\sigma} + \mathbf{v}^{1-}_{lm\sigma} c^{-}_{lm\sigma}), \tag{2.6}$$

where $b^{\pm}_{\lambda\mu\sigma}$ and $c^{\pm}_{lm\sigma}$ are scalar amplitudes, and the notation $\sum\!\!\!\!\!\!\int$ means discrete summation for discrete indices and integral for continuous indices. In this analysis, the vector field $\mathbf{v}$ is solved by obtaining the unknown coefficients $c^{+}_{lm\sigma}$ and $c^{-}_{lm\sigma}$.

2.3 General reflection relations at the particle and the conduit surface

In the next step, we consider an inhomogeneous boundary condition at the particle-surface. We only consider Dirichlet conditions though other linear conditions can also be analyzed by this general technique. Accordingly, we assume that the vector field $\mathbf{v}$ at $\alpha_1 = a_1$ is $\mathbf{V}(\beta_1, \gamma_1)$ which is a function of β_1 and γ_1. We can express $\mathbf{V}(\beta_1, \gamma_1)$ in two different ways. Firstly, considering the completeness of the orthogonal vector function $\mathbf{e}^{1}_{lms}$ and invertibility of $\mathbf{S}^{1}$, one can write $\mathbf{V}(\beta_1, \gamma_1)$ as a linear combination

$$\mathbf{V}(\beta_1, \gamma_1) = \mathbf{S}^{1}(a_1, \beta_1, \gamma_1) \cdot \sum_{lms} \mathbf{e}^{1}_{lms} a_{lms}, \tag{2.7}$$

where a_{lms}'s are the amplitudes. Secondly, $\mathbf{V}(\beta_1, \gamma_1)$ can also be obtained from the vector field $\mathbf{v}$ in eq.2.6. By combining eqs.2.2 and 2.6, and by setting $\alpha_1 = a_1$, we determine

$$\mathbf{V}(\beta_1, \gamma_1) = \mathbf{S}^1(a_1, \beta_1, \gamma_1) \cdot \sum_{lms\sigma} \mathbf{e}^1_{lms}[f^{1+}_{lms\sigma}(a_1)c^+_{lm\sigma} + f^{1-}_{lms\sigma}(a_1)c^-_{lm\sigma}]. \tag{2.8}$$

Hence, by comparing eqs.2.7 and 2.8, one can find a relation between a_{lms}, $c^+_{lm\sigma}$ and $c^-_{lm\sigma}$

$$\sum_{\sigma}[f^{1-}_{lms\sigma}(a_1)c^-_{lm\sigma} + f^{1+}_{lms\sigma}(a_1)c^+_{lm\sigma}] = a_{lms}. \tag{2.9}$$

For a given inhomogeneous Dirichlet condition at the particle-fluid interface, a_{lms} is known. As a result, eq.2.9 serves as one of the constraint equations required for determination of the unknown coefficients $c^-_{lm\sigma}$ and $c^+_{lm\sigma}$.

Apart from eq.2.9, another additional equation is necessary for evaluation of $c^-_{lm\sigma}$ and $c^+_{lm\sigma}$. This equation is derived from the boundary condition at the conduit where $\mathbf{v} = \mathbf{0}$ for any $\mathbf{V}(\beta_1, \gamma_1)$. To this end, we find two sets of transformation relations between the basis solutions of the particle and the conduit coordinates. For simplicity, we assume only the case where the particle is inside the conduit so that the domain is defined by $\alpha < a$ and $\alpha_1 > a_1$. In such situation, the finiteness criteria for $f^{\pm}_{\lambda\mu s\sigma}$ and $f^{1\pm}_{lms\sigma}$ ensure the existence of two transformation relations for given relative position vector $\mathbf{R}$ and relative orientation $\hat{\mathbf{e}}$ between the particle and the conduit. These transformations are

$$\mathbf{v}^{1-}_{lm\sigma}(\mathbf{r}) = \sum\!\!\!\!\!\!\int_{\lambda\mu\sigma'} \mathbf{v}^-_{\lambda\mu\sigma'}(\mathbf{r})\ T_f(\lambda\mu\sigma', lm\sigma|\mathbf{R}, \hat{\mathbf{e}}), \tag{2.10}$$

as long as α_R (the value of α associated with $\mathbf{R}$) is smaller than α (related to $\mathbf{r}$), and

$$\mathbf{v}^+_{\lambda\mu\sigma}(\mathbf{r}) = \sum_{lm\sigma'} \mathbf{v}^{1+}_{lm\sigma'}(\mathbf{r})\ T_r(\mathbf{R}, \hat{\mathbf{e}}|lm\sigma', \lambda\mu\sigma), \tag{2.11}$$

where T_f and T_r are the transformation coefficients. By substituting eq.2.10 in eq.2.6 and eq.2.11 in eq.2.5 and comparing, we determine

$$b^-_{\lambda\mu\sigma} = \sum_{lm\sigma'} T_f(\lambda\mu\sigma, lm\sigma'|\mathbf{R}, \hat{\mathbf{e}}) c^-_{lm\sigma'}, \tag{2.12}$$

and

$$c^+_{lm\sigma} = \sum\!\!\!\!\!\!\int_{\lambda\mu\sigma'} T_r(\mathbf{R}, \hat{\mathbf{e}}|lm\sigma, \lambda\mu\sigma') b^+_{\lambda\mu\sigma'}. \tag{2.13}$$

Again substituting eq.2.12 in eq.2.5 and considering no-slip at the conduit, one obtains

$$\mathbf{v}|_{\alpha=a} = \mathbf{0} = \mathbf{S} \cdot \sum\!\!\!\!\!\!\int_{\lambda\mu s\sigma} \mathbf{e}_{\lambda\mu s} [f^+_{\lambda\mu s\sigma}(a) b^+_{\lambda\mu\sigma} + f^-_{\lambda\mu s\sigma}(a) \sum_{lm\sigma'} T_f(\lambda\mu\sigma, lm\sigma'|\mathbf{R}, \hat{\mathbf{e}}) c^-_{lm\sigma'}]. \tag{2.14}$$

Hence setting the square bracketed term in eq.2.14 as zero and using eq.2.13, we can derive the additional relation between $c^+_{lm\sigma}$ and $c^-_{lm\sigma}$.

This second relation between $c^+_{lm\sigma}$ and $c^-_{lm\sigma}$ can be simplified in terms of the reflection coefficients which ensure the satisfaction of the no-slip boundary condition at the conduit surface. By combining eq.2.13 and eq.2.14, one finds

$$c^+_{lm\sigma} = -\sum_{l'm'\sigma'} \sum\!\!\!\!\!\!\int_{\lambda\mu\sigma_1\sigma_2} T_r(\mathbf{R},\hat{\mathbf{e}}|lm\sigma,\lambda\mu\sigma_1)\, R_c(\lambda\mu\sigma_1\sigma_2;a)\, T_f(\lambda\mu\sigma_2,l'm'\sigma'|\mathbf{R},\hat{\mathbf{e}})\, c^-_{l'm'\sigma'}. \tag{2.15}$$

The conduit reflection coefficients R_c can be determined if $f^\pm_{\lambda\mu s\sigma}$'s are known

$$R_c(\lambda\mu\sigma_1\sigma_2; a) = \sum_{s=0,1,2} g^+_{\lambda\mu\sigma_1 s}(a) f^-_{\lambda\mu s\sigma_2}(a), \tag{2.16}$$

where the scalar function $g^+_{\lambda\mu\sigma_1 s}(a)$ is such that the following relation can be satisfied

$$\sum_{s=0,1,2} g^+_{\lambda\mu\sigma_1 s}(a) f^+_{\lambda\mu s\sigma_2}(a) = \delta_{\sigma_1\sigma_2}. \tag{2.17}$$

The existence of $g^{+}_{\lambda\mu\sigma_1 s}$ is assured because of the linear independence of $\mathbf{v}^{+}_{\lambda\mu 0}$, $\mathbf{v}^{+}_{\lambda\mu 1}$, $\mathbf{v}^{+}_{\lambda\mu 2}$.

Finally, eq.2.9 and eq.2.15 are combined to calculate the unknown coefficients $c^{+}_{lm\sigma}$ and $c^{-}_{lm\sigma}$ so that the Dirichlet boundary condition at both particle and confinement can be satisfied simultaneously. One can eliminate $c^{+}_{lm\sigma}$ from these equations by using a second type of reflection coefficients R_p which is associated with the particle. Accordingly,

$$d_{lm\sigma} = \sum_{s} g^{1+}_{lm\sigma s}(a_1) a_{lms} = \sum_{\sigma''} R_p(lm\sigma\sigma''; a_1) c^{-}_{lm\sigma''}$$
$$- \sum_{l'm'\sigma'} \sum_{\lambda\mu\sigma_1\sigma_2}\!\!\!\!\!\!\int T_r(\mathbf{R}, \hat{\mathbf{e}}|lm\sigma, \lambda\mu\sigma_1)\ R_c(\lambda\mu\sigma_1\sigma_2; a)\ T_f(\lambda\mu\sigma_2, l'm'\sigma'|\mathbf{R}, \hat{\mathbf{e}})\ c^{-}_{l'm'\sigma'}. \quad (2.18)$$

The relation between R_p and $f^{1\pm}_{lm\sigma}$ is similar to the relation between R_c and $f^{\pm}_{\lambda\mu s\sigma}$

$$R_p(lm\sigma\sigma'; a_1) = \sum_{s=0,1,2} g^{1+}_{lm\sigma s}(a_1) f^{1-}_{lms\sigma'}(a_1), \quad (2.19)$$

where

$$\sum_{s=0,1,2} g^{1+}_{lm\sigma s}(a_1) f^{1+}_{lms\sigma'}(a_1) = \delta_{\sigma\sigma'}. \quad (2.20)$$

Hence, for a given boundary condition at the particle where $d_{lm\sigma}$ is known, we first solve eq.2.18 and then use eq.2.15 for complete solution.

In spite of apparent mathematical complexity, the key elements of the method are simple. First, we determine two sets of separable basis solutions and use the four indexed scalar functions to construct the coefficients for particle reflection R_p and confinement reflection R_c. Then two types of transformation coefficients denoted by T_f and T_r are evaluated. Finally, we solve the vector field $\mathbf{v}$ by calculating the amplitudes $c^{-}_{lm\sigma}$ and $c^{+}_{lm\sigma}$ from eq.2.18 and eq.2.15, respectively. In order to keep the analysis simple, in this paper we specifically assume that 1) boundary conditions

are Dirichlet, 2) a single surface forms the confinement, 3) the particle is inside the vessel and 4) only a single particle is present in the system. Fortunately, with minor modifications, the technique can also be applied to a far more general scenario where all these assumptions are relaxed.

CHAPTER 3
GENERAL STOKESIAN SOLUTION FOR FLOW AROUND A SPHERE IN A CYLINDER

To analyze creeping motion of a spherical particle inside a cylindrical vessel, we treat Stokes equation as the second order vector equation mentioned in section 2:

$$\eta \nabla^2 \mathbf{v} = \nabla p. \tag{3.1}$$

$$\nabla \cdot \mathbf{v} = 0. \tag{3.2}$$

Here, η is viscosity, $\mathbf{v}$ is velocity-field and p is pressure. The Dirichlet conditions are specified at the surfaces of the sphere and the cylinder where $\mathbf{v}$ is known.

Following the outlined procedure, we find separable basis velocities for Stokes equation in cylindrical and spherical coordinates according to eqs.2.1 and 2.2, and calculate R_c and R_p. Then, we show how to derive corresponding T_f and T_r.

The analysis can be drastically simplified if one takes advantage of two well-known symmetries. In the next two subsections, we show how to use these two symmetries.

3.1 The recurrence curl relation between the basis solutions of Stokes equation

Using vector identities, the Stokes equations 3.1 and 3.2 can be rewritten in an equivalent form

$$\nabla \times \nabla \times \nabla \times \mathbf{v} = \mathbf{0}. \tag{3.3}$$

From the recurrence of the operator $\nabla\times$ in eq.3.3, one can draw the following conclusion about the solutions of Stokes equation: if one finds a solution $\mathbf{v}_{\text{prs}}$ for which $\nabla \times \nabla \times \mathbf{v}_{\text{prs}}$ is non-trivial, then $\mathbf{v}_{\text{vor}} = q\nabla \times \mathbf{v}_{\text{prs}}$ and $\mathbf{v}_{\text{pot}} = q\nabla \times \mathbf{v}_{\text{vor}}$ (with q being a constant) are also two independent solutions. This recurrence symmetry of Stokesian

fields is well known [77, 111] and $\mathbf{v}_{\rm prs}$, $\mathbf{v}_{\rm vor}$, $\mathbf{v}_{\rm pot}$ are similar to the pressure, vorticity and potential solutions described in [112]. This recurrence symmetry has a two-fold advantage.

Firstly, due to the recurrence relation, the construction of the basis solutions becomes easier — we do not require to individually derive all three solutions correspond to $\sigma = 0, 1, 2$. We just obtain the one which gives non-trivial field when operated twice by the Curl operator and assign one value of σ for the solution. The other two basis fields corresponding to the other two values of σ are derived by taking Curl and double Curl of the first solution. Accordingly, we follow the convention where $\mathbf{v}^{+}_{\lambda\mu 2}$, $\mathbf{v}^{-}_{\lambda\mu 0}$, $\mathbf{v}^{1+}_{lm2}$ and $\mathbf{v}^{1-}_{lm0}$ have non-trivial double Curl and

$$\mathbf{v}^{-}_{\lambda\mu 1} = q^{-}\nabla \times \mathbf{v}^{-}_{\lambda\mu 0}, \tag{3.4}$$

$$\mathbf{v}^{-}_{\lambda\mu 2} = q^{-}\nabla \times \mathbf{v}^{-}_{\lambda\mu 1}, \tag{3.5}$$

$$\mathbf{v}^{+}_{\lambda\mu 1} = q^{+}\nabla \times \mathbf{v}^{+}_{\lambda\mu 2}, \tag{3.6}$$

$$\mathbf{v}^{+}_{\lambda\mu 0} = q^{+}\nabla \times \mathbf{v}^{+}_{\lambda\mu 1}, \tag{3.7}$$

$$\mathbf{v}^{1-}_{lm1} = q^{-}_{1}\nabla \times \mathbf{v}^{1-}_{lm0}, \tag{3.8}$$

$$\mathbf{v}^{1-}_{lm2} = q^{-}_{1}\nabla \times \mathbf{v}^{1-}_{lm1}, \tag{3.9}$$

$$\mathbf{v}^{1+}_{lm1} = q^{+}_{1}\nabla \times \mathbf{v}^{1+}_{lm2}, \tag{3.10}$$

$$\mathbf{v}^{1+}_{lm0} = q^{+}_{1}\nabla \times \mathbf{v}^{1+}_{lm1}, \tag{3.11}$$

where $q^{\pm}$, $q^{\pm}_{1}$ are four constants which are chosen as per convenience. Among the solutions defined in eq.3.4–3.11, the ones with $\sigma = 1$ are solenoidal harmonic vector fields whereas remaining solutions ($\mathbf{v}^{-}_{\lambda\mu 2}$, $\mathbf{v}^{+}_{\lambda\mu 0}$, $\mathbf{v}^{1-}_{lm2}$, $\mathbf{v}^{1+}_{lm0}$) are potential fields.

The second benefit of the recurrence relation is simplification of the derivation

of T_f and T_r. By taking Curl and double Curl of eq.2.10 and using eqs.3.4–3.5 and 3.8–3.9, we find

$$T_f(\lambda\,\mu\,\sigma'{+}j, l\,m\,\sigma{+}j) = (q_1^-/q^-)^j\ T_f(\lambda\mu\sigma', lm\sigma) \qquad \text{for} \qquad j < 2-max(\sigma',\sigma) \quad (3.12)$$

and

$$T_f(\lambda\mu\sigma', lm\sigma) = 0 \qquad \text{for} \qquad \sigma' < \sigma, \quad (3.13)$$

where max means the maximum of the arguments, and $\mathbf{R}$ and $\hat{\mathbf{e}}$ are omitted for notational simplicity. Hence, T_f for all σ and σ' can be defined by only three coefficients instead of nine — we just have to determine only $T_f(\lambda\mu 0, lm0)$, $T_f(\lambda\mu 1, lm0)$, $T_f(\lambda\mu 2, lm0)$ in terms of which the remaining non-zero coefficients can be expressed. Similarly, we can also simplify T_r by taking Curl and double Curl of eq.2.11 and using eqs.3.6–3.7 and 3.10–3.11

$$T_r(l\,m\,\sigma{+}j, \lambda\,\mu\,\sigma'{+}j) = (q_1^+/q^+)^j\ T_r(lm\sigma, \lambda\mu\sigma') \qquad \text{for} \qquad j < 2-max(\sigma',\sigma) \quad (3.14)$$

and

$$T_r(lm\sigma, \lambda\mu\sigma') = 0 \qquad \text{for} \qquad \sigma' > \sigma. \quad (3.15)$$

For these coefficients, we just evaluate $T_r(lm0, \lambda\mu 2)$, $T_r(lm1, \lambda\mu 2)$, $T_r(lm2, \lambda\mu 2)$, and utilize eq.3.14 to find other non-zero coefficients for different σ and σ'.

3.2 Normalization by Oseen tensor

In the previous section, we show that if somehow we can derive the expression for Stokesian solutions with non-trivial double Curl (i.e. $\mathbf{v}^+_{\lambda\mu 2}$, $\mathbf{v}^-_{\lambda\mu 0}$, $\mathbf{v}^{1+}_{lm2}$, $\mathbf{v}^{1-}_{lm0}$), we can complete the set of basis fields for different σ very easily. However, there is no unique way to construct aforementioned fields because of the gauge invariance. We can always add irrotational or solenoidal-harmonic vector functions with $\mathbf{v}^+_{\lambda\mu 2}$, $\mathbf{v}^-_{\lambda\mu 0}$,

$\mathbf{v}^{1+}_{lm2}$, $\mathbf{v}^{1-}_{lm0}$ without contradicting their definitions. In this section, we use another symmetry of the Stokesian solutions for unique representation of these basis fields. In the process, we take advantage of the inherent gauge invariance to simplify the subsequent analysis.

Among the Stokesian basis, the ones correspond to a potential field is the only solutions which are not affected by the gauge fields. So they can be uniquely defined (besides normalization constants) as a gradient of a harmonic scalar field.

$$\mathbf{v}^{-}_{\lambda\mu 2} = \nabla\Phi^{-}_{\lambda\mu}, \tag{3.16}$$

$$\mathbf{v}^{+}_{\lambda\mu 0} = \nabla\Phi^{+}_{\lambda\mu}, \tag{3.17}$$

$$\mathbf{v}^{1-}_{lm2} = \nabla\Phi^{1-}_{lm}, \tag{3.18}$$

$$\mathbf{v}^{1+}_{lm0} = \nabla\Phi^{1+}_{lm}, \tag{3.19}$$

where $\Phi^{\pm}_{\lambda\mu}$, $\Phi^{1\pm}_{lm}$ are separable solutions for Laplace equation in respective coordinates

$$\Phi^{-}_{\lambda\mu}=\frac{K_\mu(\lambda\rho)e^{i(\mu\beta+\lambda z)}}{A^{-}_{\lambda\mu}} \tag{3.20}$$

$$\Phi^{+}_{\lambda\mu}=\frac{I_\mu(\lambda\rho)e^{i(\mu\beta+\lambda z)}}{A^{+}_{\lambda\mu}} \tag{3.21}$$

$$\Phi^{1-}_{lm}=\frac{Y_{lm}(\theta,\phi)}{A^{1-}_{lm}r^{l+1}} \tag{3.22}$$

$$\Phi^{1+}_{lm}=\frac{r^l Y_{lm}(\theta,\phi)}{A^{1+}_{lm}}. \tag{3.23}$$

In eq.3.20–3.23 K_μ and I_μ are two kinds of modified Bessel functions of integer order μ, Y_{lm} are normalized spherical harmonics, and $A^{\pm}_{\lambda\mu}$, $A^{1\pm}_{lm}$ are scaling constants. If we set

$$A^{-}_{\lambda\mu} = 4\pi^2/A^{+}_{\lambda\mu}, \tag{3.24}$$

$$A_{lm}^{1-} = (2l+1)/A_{lm}^{1+}, \tag{3.25}$$

then by using the properties of $\Phi_{\lambda\mu}^{\pm}$ and $\Phi_{lm}^{1\pm}$, one can prove that the Greens function G for Laplace equation is as below:

$$G(\mathbf{r}-\mathbf{r}') = \frac{1}{4\pi|\mathbf{r}-\mathbf{r}'|} = \int_{-\infty}^{\infty} \sum_{\mu=-\infty}^{\infty} \Phi_{\lambda\mu}^{+*}(\mathbf{r}')\Phi_{\lambda\mu}^{-}(\mathbf{r})d\lambda = \sum_{l=1}^{\infty}\sum_{m=-l}^{l} \Phi_{lm}^{1+*}(\mathbf{r}')\Phi_{lm}^{1-}(\mathbf{r}), \tag{3.26}$$

where $\mathbf{r}$ is position of the observation point and $\mathbf{r}'$ is the position of a source. Two vectors $\mathbf{r}$ and $\mathbf{r}'$ are such that $\rho > \rho'$ and $r > r'$ where primed coordinates relate to $\mathbf{r}'$.

We recognize the tensor $\nabla\nabla' G$ (with ∇' being the gradient in $\mathbf{r}'$ space) as

$$\nabla\nabla' G = \int_{-\infty}^{\infty} \sum_{\mu=-\infty}^{\infty} \mathbf{v}_{\lambda\mu 0}^{+*}(\mathbf{r}')\mathbf{v}_{\lambda\mu 2}^{-}(\mathbf{r})d\lambda = \sum_{l=1}^{\infty}\sum_{m=-l}^{l} \mathbf{v}_{lm0}^{1+*}(\mathbf{r}')\mathbf{v}_{lm2}^{1-}(\mathbf{r}), \tag{3.27}$$

and relate it to Oseen tensor $\mathbf{T}$ in three equivalent ways

$$\nabla \times \nabla \times \mathbf{T} = -\nabla\nabla' G \tag{3.28}$$

$$\nabla' \times \nabla' \times \mathbf{T} = -\nabla\nabla' G \tag{3.29}$$

$$\nabla \times \nabla' \times \mathbf{T} = \nabla\nabla' G \tag{3.30}$$

where

$$\mathbf{T}(\mathbf{r}-\mathbf{r}') = \frac{1}{8\pi|\mathbf{r}-\mathbf{r}'|}[\mathbf{I} - (\mathbf{r}-\mathbf{r}')(\mathbf{r}-\mathbf{r}')/|\mathbf{r}-\mathbf{r}'|^2]. \tag{3.31}$$

From eqs.3.4–3.11, 3.27 and 3.28–3.30 it can be shown that we can construct unique $\mathbf{v}_{\lambda\mu 2}^{+}$, $\mathbf{v}_{\lambda\mu 0}^{-}$, $\mathbf{v}_{lm2}^{1+}$, $\mathbf{v}_{lm0}^{1-}$ by fixing the gauge fields so that when $q^{+*} = q^{-} = q_1^{+*} = q_1^{-} = i$

$$\mathbf{T}(\mathbf{r}-\mathbf{r}') = \sum\!\!\!\!\!\!\int_{\lambda\mu\sigma'} \mathbf{v}_{\lambda\mu\sigma'}^{+*}(\mathbf{r}')\mathbf{v}_{\lambda\mu\sigma'}^{-}(\mathbf{r}) = \sum_{lm\sigma} \mathbf{v}_{lm\sigma}^{1+*}(\mathbf{r}')\mathbf{v}_{lm\sigma}^{1-}(\mathbf{r}). \tag{3.32}$$

We impose the additional constraint described as eq.3.32 on $\mathbf{v}^{+}_{\lambda\mu 2}$, $\mathbf{v}^{-}_{\lambda\mu 0}$, $\mathbf{v}^{1+}_{lm2}$, $\mathbf{v}^{1-}_{lm0}$ to render the uniqueness of the basis solutions for chosen values of $A^{+}_{\lambda\mu}$ and A^{1+}_{lm}.

If eq.3.32 is used to define the basis solutions, a major simplification can be achieved in the analysis. By expanding $\mathbf{v}^{1-}_{lm\sigma}(\mathbf{r})$ in terms of $\mathbf{v}^{-}_{\lambda\mu\sigma'}(\mathbf{r})$ as in eq.2.10 and $\mathbf{v}^{+*}_{\lambda\mu\sigma'}(\mathbf{r}')$ in terms of $\mathbf{v}^{1+*}_{lm\sigma}(\mathbf{r}')$ as in eq.2.11 for same conduit-particle configuration (i.e. for same $\mathbf{R}$ and $\hat{\mathbf{e}}$), and equating two summation series of outer products in eq.3.32, we get

$$\sum\!\!\!\!\!\!\int_{\lambda\mu\sigma'} \sum_{lm\sigma} \mathbf{v}^{1+*}_{lm\sigma}(\mathbf{r}') T^{*}_{r}(\mathbf{R}|lm\sigma,\lambda\mu\sigma') \mathbf{v}^{-}_{\lambda\mu\sigma'}(\mathbf{r}) = \sum\!\!\!\!\!\!\int_{\lambda\mu\sigma'} \sum_{lm\sigma} \mathbf{v}^{1+*}_{lm\sigma}(\mathbf{r}') T_{f}(\lambda\mu\sigma', lm\sigma|\mathbf{R}) \mathbf{v}^{-}_{\lambda\mu\sigma'}(\mathbf{r}) \tag{3.33}$$

The above equation is true for all possible $\mathbf{r}$ and $\mathbf{r}'$ as long as $\rho_R < \rho$ (ρ_R being related to $\mathbf{R}$). Such general equality is only possible if

$$T_{f}(\lambda\mu\sigma', lm\sigma|\mathbf{R}) = T^{*}_{r}(\mathbf{R}|lm\sigma,\lambda\mu\sigma'). \tag{3.34}$$

Such relation between two types of transformation coefficients is an alternative version of well known reciprocal theorem. The benefit of eq.3.34 is that if T_r is calculated T_f is known immediately.

3.2.1 Basis solutions and transformation coefficients

In this subsection, we integrate all elements of the analysis that is presented so far. The theoretical results summarized here provide all necessary components of our simulation.

By combining eqs.3.4–3.7, 3.16–3.25, 3.32 and setting $A^{+}_{\lambda\mu} = A^{-}_{\lambda\mu} = 2\pi$, $q^{+} = q^{-*} = i$, we derive $\mathbf{v}^{\pm}_{\lambda\mu\sigma}$ in the form described by eq.2.1. Accordingly, we first find

$$\mathbf{e}_{\lambda\mu 0} = \hat{\mathbf{e}}^{-} \, \frac{e^{i(\mu\beta+\lambda z)}}{2\pi} \tag{3.35}$$

$$\mathbf{e}_{\lambda\mu 1} = \hat{\mathbf{e}}^{+}\ \frac{e^{i(\mu\beta+\lambda z)}}{2\pi} \tag{3.36}$$

$$\mathbf{e}_{\lambda\mu 2} = \hat{\mathbf{e}}_z \frac{e^{i(\mu\beta+\lambda z)}}{2\pi}, \tag{3.37}$$

where

$$\hat{\mathbf{e}}^{-} = \frac{\hat{\mathbf{e}}_x - i\hat{\mathbf{e}}_y}{\sqrt{2}} e^{i\beta} \tag{3.38}$$

$$\hat{\mathbf{e}}^{+} = \frac{\hat{\mathbf{e}}_x + i\hat{\mathbf{e}}_y}{\sqrt{2}} e^{-i\beta}, \tag{3.39}$$

with $\hat{\mathbf{e}}_z$ being the unit vector along the axis of the conduit, and $\hat{\mathbf{e}}_x$ and $\hat{\mathbf{e}}_y$ being mutually perpendicular unit vector in a plane perpendicular to z. Then we complete the description of $\mathbf{v}^{\pm}_{\lambda\mu\sigma}$ by expressing $f^{\pm}_{\lambda\mu s\sigma}$ in terms of the σ+1, s+1-th element of 3×3 matrices $\mathsf{F}^{\pm}_{\lambda\mu}$

$$\mathsf{F}^{+}_{\lambda\mu} = \begin{bmatrix} \frac{\lambda I_{\mu+1}(\lambda\rho)}{\sqrt{2}} & \frac{iI_{\mu+1}(\lambda\rho)}{\sqrt{2}} & \frac{\rho(I_{\mu+2}(\lambda\rho)+I_{\mu}(\lambda\rho))}{4\sqrt{2}} \\ \frac{\lambda I_{\mu-1}(\lambda\rho)}{\sqrt{2}} & -\frac{iI_{\mu-1}(\lambda\rho)}{\sqrt{2}} & \frac{\rho(I_{\mu}(\lambda\rho)+I_{\mu-2}(\lambda\rho))}{4\sqrt{2}} \\ i\lambda I_{\mu}(\lambda\rho) & 0 & i\frac{\lambda\rho I_{\mu+1}(\lambda\rho)+\lambda\rho I_{\mu-1}(\lambda\rho)+2I_{\mu}(\lambda\rho)}{4\lambda} \end{bmatrix},$$

$$\mathsf{F}^{-}_{\lambda\mu} = \begin{bmatrix} \frac{\rho(K_{\mu+2}(\lambda\rho)+K_{\mu}(\lambda\rho))}{4\sqrt{2}} & \frac{iK_{\mu+1}(\lambda\rho)}{\sqrt{2}} & -\frac{\lambda K_{\mu+1}(\lambda\rho)}{\sqrt{2}} \\ \frac{\rho(K_{\mu}(\lambda\rho)+K_{\mu-2}(\lambda\rho))}{4\sqrt{2}} & -\frac{iK_{\mu-1}(\lambda\rho)}{\sqrt{2}} & -\frac{\lambda K_{\mu-1}(\lambda\rho)}{\sqrt{2}} \\ -i\frac{\lambda\rho K_{\mu+1}(\lambda\rho)+\lambda\rho K_{\mu-1}(\lambda\rho)-2K_{\mu}(\lambda\rho)}{4\lambda} & 0 & i\lambda K_{\mu}(\lambda\rho) \end{bmatrix}, \tag{3.40}$$

and proving $\mathbf{S}$ to be the identity tensor $\mathbf{I}$. The conduit reflection is evaluated using $\mathsf{F}^{\pm}_{\lambda\mu}$,

$$\mathsf{R}_c(\lambda\mu; a) = [\mathsf{F}^{+}_{\lambda\mu}(a)]^{-1}[\mathsf{F}^{-}_{\lambda\mu}(a)], \tag{3.41}$$

where the σ_1+1, σ_2+1-th element of $\mathsf{R}_c(\lambda\mu; a)$ represents reflection coefficients $R_c(\lambda\mu\sigma_1\sigma_2; a)$.

In a similar way, combining eqs.3.8–3.11, 3.16–3.25, 3.32 and setting $A^{1+}_{lm} = 1$,

$A^{1-}_{lm} = 2l+1$, $q^{1+} = q^{1-*} = i$, we obtain $\mathbf{v}^{1\pm}_{lm\sigma}$ defined in eq.2.2. We find $\mathbf{S}_1 = \mathbf{I}$,

$$\mathbf{e}^1_{lm0} = \hat{\mathbf{e}}_r Y_{lm} \tag{3.42}$$

$$\mathbf{e}^1_{lm1} = r\hat{\mathbf{e}}_r \times \nabla Y_{lm} \tag{3.43}$$

$$\mathbf{e}^1_{lm2} = r\nabla Y_{lm}, \tag{3.44}$$

where $1<l<\infty$, $-l<m<l$, and express $f^{1\pm}_{lms\sigma}$ in terms of the σ+1, s+1-th element of $\mathsf{F}^{1\pm}_{lm}$

$$\mathsf{F}^{1+}_{lm}=\begin{bmatrix} lr^{l-1} & 0 & \dfrac{lr^{l+1}}{2(2l+3)} \\ 0 & \dfrac{ir^l}{l+1} & 0 \\ r^{l-1} & 0 & \dfrac{(l+3)r^{l+1}}{2(l+1)(2l+3)} \end{bmatrix}, \tag{3.45}$$

$$\mathsf{F}^{1-}_{lm}=\frac{1}{2l+1}\begin{bmatrix} \dfrac{(l+1)r^{-l}}{2(2l-1)} & 0 & -(l+1)r^{-l-2} \\ 0 & \dfrac{ir^{-l-1}}{l} & 0 \\ \dfrac{(l-2)r^{-l}}{2l(2l-1)} & 0 & r^{-l-2} \end{bmatrix}. \tag{3.46}$$

Then we construct

$$\mathsf{R}_p(lm;a_1) = [\mathsf{F}^{1+}_{lm}(a_1)]^{-1}[\mathsf{F}^{1-}_{lm}(a_1)], \tag{3.47}$$

to represent reflection coefficients $R_p(lm\sigma_1\sigma_2;a_1)$ as the σ_1+1, σ_2+1-th element of $\mathsf{R}_p(lm;a_1)$.

Once the basis solutions for cylindrical and spherical coordinates are derived, the transformation coefficients as defined in eq.2.10 and 2.11 are determined. For a single sphere inside a cylinder, the coordinates and origins are chosen in such a way that the relative position is given by $\mathbf{R} = R\hat{\mathbf{e}}_x$ and $\hat{\mathbf{e}}$ correspond to an orientation where θ in spherical system is measured from an axis parallel to the conduit axis. For such

configuration, from Taylor series expansion we calculate

$$T_r(lm2, \lambda\mu2) = C_{lm} M(\lambda, \mu; l, m), \tag{3.48}$$

$$T_r(lm1, \lambda\mu2) = -\frac{im}{\lambda l} C_{lm} M(\lambda, \mu; l, m), \tag{3.49}$$

$$\begin{aligned} T_r(lm0, \lambda\mu2) = & \frac{l(l-1)(2l-1) - (l^2-m^2)(l-2)}{2\lambda^2 l(2l-1)} C_{lm} M(\lambda, \mu; l, m) \\ & -\frac{R}{4\lambda^2} C_{lm}[M(\lambda, \mu; l+1, m-1) - M(\lambda, \mu; l+1, m+1)], \end{aligned} \tag{3.50}$$

where

$$M(\lambda, \mu; l, m) = \frac{2}{\sqrt{\pi}} (i\lambda)^l (i^m) I_{|m-\mu|}(\lambda R) \tag{3.51}$$

$$C_{lm} = \frac{1}{\sqrt{4(l-m)!(l+m)!(2l+1)}}. \tag{3.52}$$

The derivation of these coefficients is presented in appendix 1. From the listed coefficients in eqs.3.48–3.50, one can evaluate all coefficients in T_f and T_r with the help of eqs.3.12, 3.13, 3.14, 3.15, 3.34.

CHAPTER 4

NUMERICAL IMPLEMENTATION

The main objective of our numerical simulation is to compute the hydrodynamic force and torque on the particle inside the cylinder. We relate the force and torque on the particle to its linear and angular velocities by using generalized friction tensors. In the formulation, we also include the contribution of a pressure-driven parabolic flow impending from infinity. Accordingly, one finds

$$\mathbf{f} = \mathbf{F}^{tt} \cdot \mathbf{u} + \mathbf{F}^{tr} \cdot \boldsymbol{\omega} + \mathbf{f}^{p} + \mathbf{f}^{ex}, \tag{4.1}$$

and

$$\boldsymbol{\tau} = \sum (\mathbf{F}^{rt} \cdot \mathbf{u} + \mathbf{F}^{rr} \cdot \boldsymbol{\omega}) + \boldsymbol{\tau}^{p} + \boldsymbol{\tau}^{ex}. \tag{4.2}$$

In eqs.4.1 and 4.2, $\mathbf{f}$ and $\boldsymbol{\tau}$ are the net force and torque on the particle whereas $\mathbf{u}$ and $\boldsymbol{\omega}$ are the translational and rotational velocities. The viscous force and torque on a fixed sphere in presence of a parabolic flow are given by $\mathbf{f}^{p}$ and $\boldsymbol{\tau}^{p}$, and the external force and torque on the suspended body are $\mathbf{f}^{ex}$ and $\boldsymbol{\tau}^{ex}$. The second order tensors $\mathbf{F}^{tt}$, $\mathbf{F}^{rr}$, $\mathbf{F}^{tr}$ and $\mathbf{F}^{rt}$ are friction tensors with $\mathbf{F}^{tr}$ being the transpose of $\mathbf{F}^{rt}$. In our analysis, we first evaluate $\mathbf{F}^{tt}$, $\mathbf{F}^{rr}$, $\mathbf{F}^{tr}$, $\mathbf{F}^{rt}$, $\mathbf{f}^{p}$ and $\boldsymbol{\tau}^{p}$. Then from eqs.4.1 and 4.2 we also calculate $\mathbf{u}$ and $\boldsymbol{\omega}$ for freely moving particle where $\mathbf{f}^{ex} = \mathbf{f} = \mathbf{0}$ and $\boldsymbol{\tau} = \boldsymbol{\tau}^{ex} = \mathbf{0}$.

We find the aforementioned quantities by solving the linear systems of equations in eq.2.18 which relates $c^{-}_{l'm'\sigma'}$ to known $d_{lm\sigma}$. One can invert these equations and gets

$$c^{-}_{l'm'\sigma'} = \sum_{lm\sigma} L(l'm'\sigma', lm\sigma) d_{lm\sigma}. \tag{4.3}$$

The coupling constants $L(l'm'\sigma', lm\sigma)$ correspond to the inverse of the relation in

eq.2.18

$$\sum_{lm\sigma} L(l'm'\sigma', lm\sigma)M(lm\sigma, l''m''\sigma'') = \delta_{l'l''}\delta_{m'm''}\delta_{\sigma'\sigma''}, \tag{4.4}$$

where

$$\begin{aligned} &M(lm\sigma, l''m''\sigma'') = R_p(lm\sigma\sigma''; a_1)\delta_{ll''}\delta_{mm''} \\ &-\sum_{\sigma_1\sigma_2}\sum_{\mu=-\infty}^{\infty}\int_{-\infty}^{\infty} T_r(lm\sigma, \lambda\mu\sigma_1)\ R_c(\lambda\mu\sigma_1\sigma_2; a)\ T_f(\lambda\mu\sigma_2, l''m''\sigma'')\ d\lambda. \end{aligned} \tag{4.5}$$

Often L is referred as the grand friction matrix whereas M is the grand mobility matrix. The components of $\mathbf{F}^{tt}$, $\mathbf{F}^{rr}$, $\mathbf{F}^{tr}$, $\mathbf{F}^{rt}$, $\mathbf{f}^{p}$, $\boldsymbol{\tau}^{p}$ are related to various linear combinations of $L(l'm'\sigma', lm\sigma)$. For example, the axial translational friction F^{tt}_{zz} is proportional to the element $L(100, 100)$. Similarly, both radial ($F^{tt}_{\rho\rho}$) and azimuthal ($F^{tt}_{\beta\beta}$) frictions are linear combinations of $L(110, 110)$, $L(1\ {-}10, 1\ {-}10)$, $L(1\ {-}10, 110)$, $L(110, 1\ {-}10)$.

So in our simulation, we first compute M by numerically integrating over λ and summing over σ_1, σ_2 and μ. Then we invert the matrix representing M to calculate L. Finally, the relevant quantities are extracted from different linear combinations of $L(l'm'\sigma', lm\sigma)$. However, there can be numerical errors because of inherent approximations in the process. Firstly, the construction of M is inaccurate because of involved numerical summations and integrals. Secondly, there is error in the inversion of M because we truncate the infinite set of coefficients at some finite value. In the next two subsections, we present representative convergence tests to provide an estimate of these two types of error, respectively, for a few critical elements.

4.1 Errors in construction of the grand mobility matrix

We identify three numerical approximations in the evaluation of M. First of all, the interval length for the numerical integration in λ is considered $\delta\lambda$ which is finite. Then numerical integration is truncated at certain Λ_{max} instead of ∞ so that the

integration on λ is from $-\Lambda_{max}$ to Λ_{max}. Finally, the infinite summation over μ is truncated so that in simulation the summation is actually from $-\mu_{max}$ to μ_{max}. Hence, we choose the diagonal elements of $\mathbf{F}^{tt}$ as representative cases and study convergences on $\delta\lambda$, Λ_{max} and μ_{max}. We choose these particular elements because these are most crucial friction elements and at the same time more prone to convergence problems.

In Fig.4.1, the computed values of translational frictions are presented as a function of $\delta\lambda$. In this study, two configurations are considered where the particle center is either in the middle of the cylinder surface and the cylinder center or very near to the cylinder surface. In both cases, the cylinder radius a is twice of the sphere radius a_1. We employed a cubic integral scheme where we assign $\Lambda_{max} = 12.0$. The other numerical parameter μ_{max} is assumed to be 12. The figure shows that the convergence of the curves to a particular value is very fast. When the particle is away from the wall with $R = 0.5a_1$ the convergence is relatively better. We check that the order of convergence for low $\delta\lambda$ is between 3 to 4.

Next, we focus on the convergence of the same quantities with respect to Λ_{max} for the same configurations. For these studies, we consider $\delta\lambda = 0.1$ and $\mu_{max} = 12$. These results are presented in Fig.4.2 from which one can conclude that the values converge well at $\Lambda_{max} = 5.0$. Again, we find the convergence is better for $R = 0.5a_1$.

In Fig.4.3, we show how the values converge with μ_{max} where $\delta\lambda = 0.1$ and $\Lambda_{max} = 12$. It can be concluded that for $\mu_{max} = 5$, a reasonable convergence is achieved for all configurations.

We notice the common trend where the convergences are better for a particle situated in the middle where $R = 0.5a_1$ than the particle very near to the cylindrical wall. The reason behind such convergence characteristics is when the particle is near the cylinder periphery we need more cylindrical basis solutions (i.e. more Λ_{max} and μ_{max}) to describe the scattered flow-field from the particle at the conduit surface. The number of required cylindrical basis is related to the angle sustained by the particle

at the axis of the cylinder — more solutions are needed for less angle. Hence further the particle is situated from the periphery, less Λ_{max} and μ_{max} is necessary.

This convergence property is advantageous for simulation because we can efficiently analyze the cases where the particle is somewhere between the cylinder surface and cylinder center and our method is the only means for computation. This does not imply that the other cases can not be simulated by the presented technique — for all cases the simulation time for one configuration is order of a few seconds. This only suggests that this procedure is extra useful in the situations where asymptotic methods does not work.

4.2 Approximation in solution of the linear systems of equation

Ideally, in the matrix $M(l'm'\sigma', lm\sigma)$, the integer indices l' and l varies from 1 to ∞. In practice, the infinite dimensional matrix M is truncated to a certain dimension and then inverted to evaluate M approximately. Accordingly, we assign a maximum value l_{max} for both l and l', and construct the matrix L representing $L(l'm'\sigma', lm\sigma)$ with primed and unprimed indices corresponding to rows and columns, respectively. In that case, considering $-l' < m' < l'$, $-l < m < l$ and $\sigma, \sigma' = 0, 1, 2$, one can determine the dimension of the matrix to be $q \times q$ where $q = 3l_{max}(l_{max} + 2)$.

The error in L due to the truncation in the dimension of M can be manifested by a convergence test (known as spectral convergence) which demonstrates how the friction coefficients saturates to a certain value for increasing l_{max}. We present these results in Fig.4.4 where we plot diagonal elements of $\mathbf{F}^{tt}$ and $\mathbf{F}^{rr}$ as a function of l_{max}. We consider $a = 2a_1$ and either $R = 0.5a_1$ or $R = 0.9a_1$.

The results show that all quantities converge well at $l_{max} = 6$ which is a very small number. This is even true for usually critical cases where particle is very near to the conduit surface. For similar gap between surfaces of the particle and confinement, planar wall geometry requires $l_{max} = 16$ for reasonable convergence [77, 111]. The

reason behind this difference is simple. For a sphere near a planar wall, the angular variation in geometry is more than a sphere inside a cylinder. To resolve larger azimuthal variation around the sphere, larger l_{max} is necessary for convergence. As a result, cylindrical geometries exhibits relatively better spectral convergence than the same in planar-wall geometries. This is a major advantage for our simulation which requires less than a minute to provide a reasonable result with relative error less than 1% for a particular configuration.

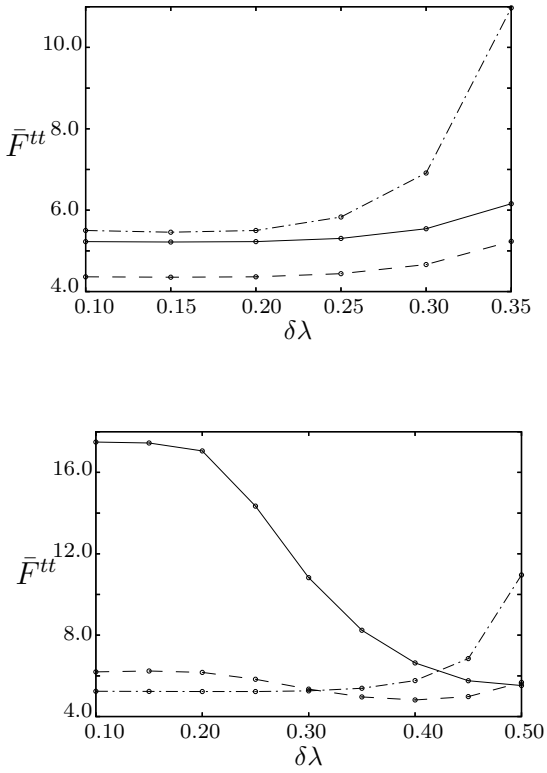

Figure 4.1: Computed values of diagonal elements of translational friction $\mathbf{F}^{tt}$ as functions of interval $\delta\lambda$ for numerical integral when $a = 2a_1$. We plot radial component $F^{tt}_{\rho\rho}$ (solid lines), azimuthal component $F^{tt}_{\beta\beta}$ (dashed line) and axial component F^{tt}_{zz} (dash-dot line) for moderate separation between surfaces of cylinder and sphere with $R = 0.5a_1$ (left) as well as for nearly touching configuration with $R = 0.9a_1$ (right).

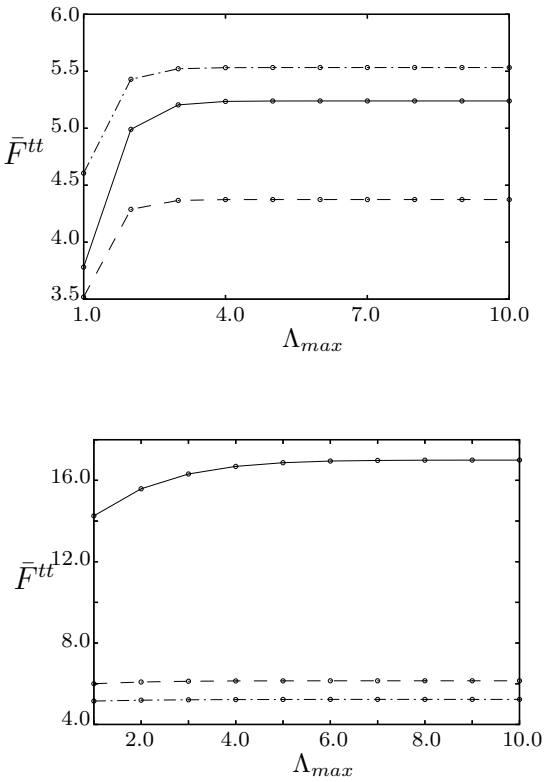

Figure 4.2: Same as Fig.4.1 except computed quantities are presented as functions of integration limit Λ_{max} instead of $\delta\lambda$ for $R = 0.5a_1$ (left) and $R = 0.9a_1$ (right).

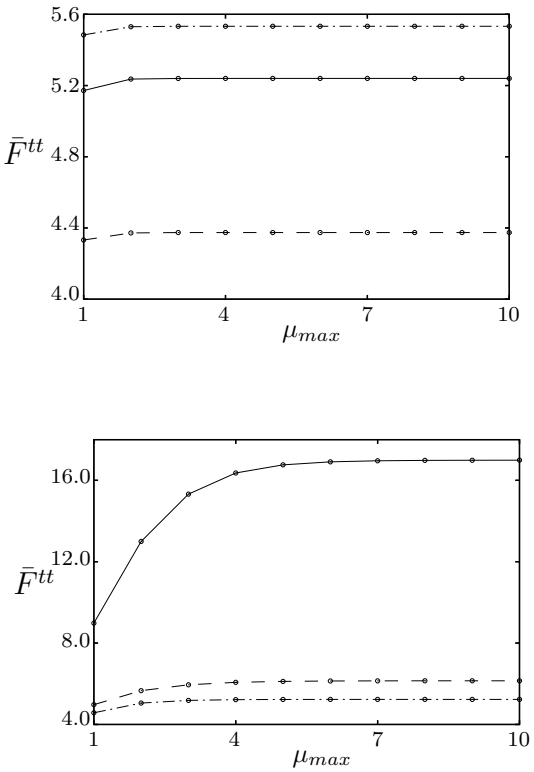

Figure 4.3: Same as Fig.4.1 except computed quantities are presented as functions of summation limit μ_{max} instead of $\delta\lambda$ for $R = 0.5a_1$ (left) and $R = 0.9a_1$ (right).

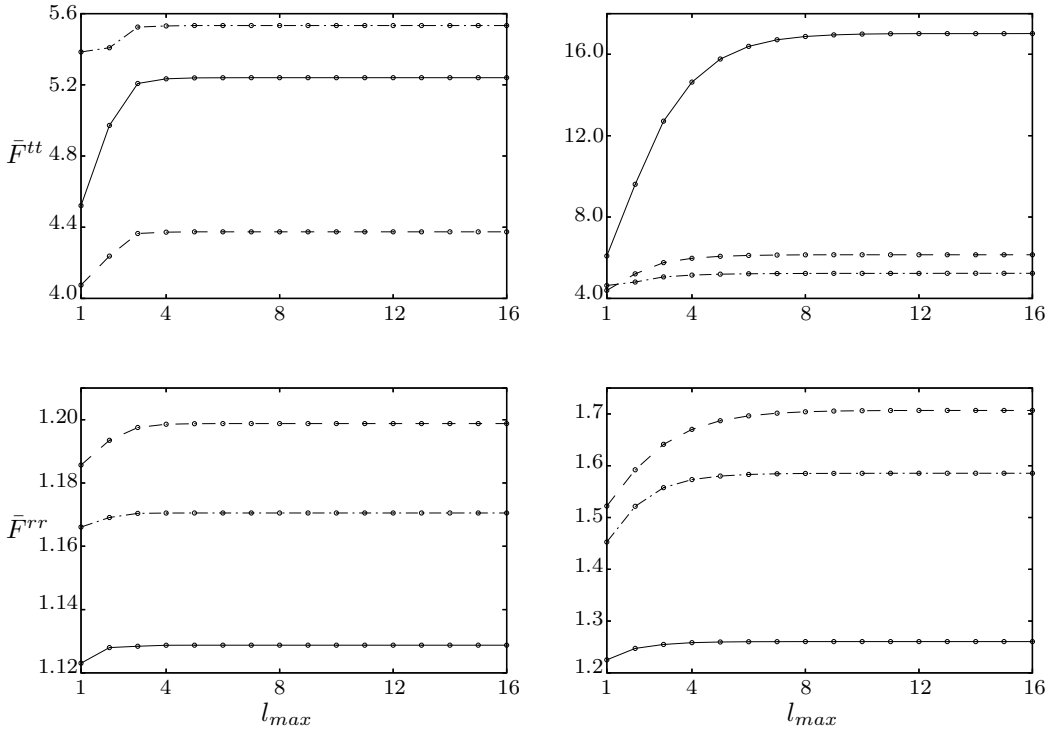

Figure 4.4: Computed values of diagonal elements of translational friction $\mathbf{F}^{tt}$ and rotational friction $\mathbf{F}^{rr}$ as functions of l_{max} representing number of basis functions considered in the simulation. The configurations and line types for radial, azimuthal and axial components are same as Fig.4.1.

CHAPTER 5
HYDRODYNAMIC RESISTANCE IN QUIESCENT FLUID INSIDE A CYLINDER

We apply the simulation algorithm to comprehensively describe force and torque on a sphere due to its motion in a quiescent fluid in terms of friction coefficients defined in eqs.4.1 and 4.2. Because of the symmetries involved in the problem, one can prove that both $\mathbf{F}^{tt}$ and $\mathbf{F}^{rr}$ are diagonal matrices

$$\mathbf{F}^{tt} = F^{tt}_{\rho\rho}\hat{\mathbf{e}}_\rho\hat{\mathbf{e}}_\rho + F^{tt}_{\beta\beta}\hat{\mathbf{e}}_\beta\hat{\mathbf{e}}_\beta + F^{tt}_{zz}\hat{\mathbf{e}}_z\hat{\mathbf{e}}_z, \tag{5.1}$$

$$\mathbf{F}^{rr} = F^{rr}_{\rho\rho}\hat{\mathbf{e}}_\rho\hat{\mathbf{e}}_\rho + F^{rr}_{\beta\beta}\hat{\mathbf{e}}_\beta\hat{\mathbf{e}}_\beta + F^{rr}_{zz}\hat{\mathbf{e}}_z\hat{\mathbf{e}}_z, \tag{5.2}$$

where $\hat{\mathbf{e}}_\rho$, $\hat{\mathbf{e}}_\beta$, $\hat{\mathbf{e}}_z$ are unit vectors along radial, azimuthal and axial directions. The translation-rotation coupling tensors $\mathbf{F}^{tr}$ and $\mathbf{F}^{rt}$, on the other hand, have the following form

$$\mathbf{F}^{tr} = G\hat{\mathbf{e}}_\beta\hat{\mathbf{e}}_z + G'\hat{\mathbf{e}}_z\hat{\mathbf{e}}_\beta, \tag{5.3}$$

$$\mathbf{F}^{rt} = G'\hat{\mathbf{e}}_\beta\hat{\mathbf{e}}_z + G\hat{\mathbf{e}}_z\hat{\mathbf{e}}_\beta, \tag{5.4}$$

which shows that $\mathbf{F}^{tr}$ and $\mathbf{F}^{rt}$ are transpose to each other. Hence, it is possible to analyze the dynamics of the particle in a stagnant fluid inside a cylinder, if one determines eight friction coefficients: $F^{tt}_{\rho\rho}$, $F^{tt}_{\beta\beta}$, F^{tt}_{zz}, $F^{rr}_{\rho\rho}$, $F^{rr}_{\beta\beta}$, F^{rr}_{zz}, G, G'. We evaluate these scalar quantities for various configurations defined by non-dimensional lengths parameters $R/(a-a_1)$ and a/a_1. We especially select those cases which are particularly difficult to be investigated by available asymptotic methods.

5.1 Force on a translating sphere

In Fig.5.1, nondimensional components of $\mathbf{F}^{tt}$ are presented where the quantities are normalized by the Stokesian friction of the sphere in free-space:

$$\bar{F}^{tt}_{ii} = \frac{F^{tt}_{ii}}{6\pi a_1 \eta}, \tag{5.5}$$

with i being either ρ or β or z. We plot $\bar{F}^{tt}_{\rho\rho}$, $\bar{F}^{tt}_{\beta\beta}$, $\bar{F}^{tt}_{zz}$ as functions of normalized distance $R/(a-a_1)$ of the center of the sphere from the axis of the cylinder so that the nondimensional distance is always between 0 and 1. In the figures, the ratio a/a_1 varies as a parameter for different curves. We especially chose the intermediate values for a/a_1 for which the asymptotic methods can not be used.

If the sphere is enclosed more closely by the cylindrical surface, the friction coefficients increase because of enhanced viscous interactions. This behavior is evident in Fig.5.1 which shows higher values of friction for smaller a/a_1.

Generally, when particle is nearer to the conduit wall, hydrodynamic resistance is more due to the lubrication effects. This is why as R increases, the friction coefficients usually increase in a monotonous fashion. This general trend can be seen for $\bar{F}^{tt}_{\rho\rho}$ and $\bar{F}^{tt}_{\beta\beta}$ consistently or for $\bar{F}^{tt}_{zz}$ when $a/a_1 \gg 1$. The exception of this behavior happens when the particle is moving in axial direction, and the cylinder has small cross-section. In such cases where the sphere is substantially blocking the channel, two phenomena influence the motion of the particle. Firstly, during the axial motion, the particle acts like a piston, and a pressure difference is generated across it in axial direction. This difference in the pressure field hinders the particle. Secondly, if the sphere is very near to the conduit surface, lubrication stresses due to the relative motion between the particle and the confinement also contribute in hydrodynamic resistance. When the particle is centrally placed the pressure-difference is maximum. Any shift from this position causes a release in pressure through the widened portion of the particle-wall

gap, and its effect diminishes. On the other hand, lubrication stresses are maximum at the peripheral position. Hence, if $a \sim a_1$ we can see a non-monotonous behavior where for increasing R, $\bar{F}^{tt}_{zz}$ first decreases due to reduced pressure difference and then increases due enhanced lubrication stresses.

For a centrally situated sphere inside the cylinder, rotational symmetry dictates $\bar{F}^{tt}_{\rho\rho} = \bar{F}^{tt}_{\beta\beta}$. Actually, for such axisymmetric configuration, all translational friction components $\bar{F}^{tt}_{\rho\rho}$, $\bar{F}^{tt}_{\beta\beta}$, $\bar{F}^{tt}_{zz}$ have more or less similar values. However, when the particle is placed in an off-centered position the radial component $\bar{F}^{tt}_{\rho\rho}$ varies differently than $\bar{F}^{tt}_{\beta\beta}$ and $\bar{F}^{tt}_{zz}$. For radial motion, the sphere moves normally towards the bounding surface and encounters resistance which is inversely proportional to the gap between the approaching surfaces. The explanation is well known — lubrication fields cause the sharp increase in $\bar{F}^{tt}_{\rho\rho}$ for increase in R when the particle is at the periphery of the cylinder. Similar trend is also evident for axial and azimuthal frictions, but the increase is relatively slower for $\bar{F}^{tt}_{\beta\beta}$ and $\bar{F}^{tt}_{zz}$ than that for $\bar{F}^{tt}_{\rho\rho}$. For $\bar{F}^{tt}_{\beta\beta}$ and $\bar{F}^{tt}_{zz}$, the motion of the sphere is mainly in tangential direction of the confining wall. Such motion creates weaker lubrication field which is responsible for hydrodynamic friction varying logarithmically with inter-surface gap. The logarithmic variation is weaker than inversely proportional increase. As a result, $\bar{F}^{tt}_{\beta\beta}$ and $\bar{F}^{tt}_{zz}$ are smaller than $\bar{F}^{tt}_{\rho\rho}$ when the particle is at the periphery of the cylinder.

Between $\bar{F}^{tt}_{\beta\beta}$ and $\bar{F}^{tt}_{zz}$, the latter is higher than the former at the central position due to the developed pressure difference in piston-like axial motion. The situation reverses in peripheral position because of the lubrication fields. Lubrication effect is more prominent for the azimuthal motion compared to the axial motion. This happens because azimuthal motion is normally directed to some portion of the confinement and develop relatively stronger resistance. In contrast, the axial motion is entirely directed in a tangential direction of the vessel wall and causes weaker hydrodynamic friction.

In Fig.5.2, the normalized nondimensional components of $\mathbf{F}^{tt}$ ($\bar{F}^{tt}_{\rho\rho}$, $\bar{F}^{tt}_{\beta\beta}$, $\bar{F}^{tt}_{zz}$) are plot as functions of the ratio of the radius of the cylinder to the radius of the sphere inside the cylinder a/a_1. In the figures the normalized distance $R/(a-a_1)$ of the center of the sphere from the axis of the cylinder varies as a parameter for different curves. The range of a/a_1 is specifically chosen to be between 2 and 5 to get results for the intermediate regions where the asymptotic methods can not give results. Fig.5.2 indicates similar conclusions as Fig.5.1.

5.2 Torque on a rotating sphere

The components of the rotational friction tensor $\mathbf{F}^{rr}$ is normalized by the value corresponding to a sphere in unbounded fluid

$$\bar{F}^{rr}_{ii} = \frac{F^{rr}_{ii}}{8\pi a_1^3 \eta}, \tag{5.6}$$

where i is either ρ or β or z. In Fig.5.3, the non-dimensional quantities $\bar{F}^{rr}_{\rho\rho}$, $\bar{F}^{rr}_{\beta\beta}$, $\bar{F}^{rr}_{zz}$ are presented as functions of $R/(a-a_1)$ for different a/a_1.

All the normalized components of $\mathbf{F}^{rr}$ monotonously increase with increasing $R/(a-a_1)$ and decreasing a/a_1 because such changes in $R/(a-a_1)$ and a/a_1 enhance viscous interactions due to closer proximity between the particle and the conduit surfaces. For small gap between these two bodies, lubrication effect influences the hydrodynamic behavior. As rotation produces a predominantly tangential relative motion between the touching surfaces, the resistance to the motion due to the lubrication contribution varies logarithmically with the inter-surface gap. Thus, we observe a slower increase in $\bar{F}^{rr}_{\rho\rho}$, $\bar{F}^{rr}_{\beta\beta}$, $\bar{F}^{rr}_{zz}$ with increasing $R/(a-a_1)$ compared to the behavior of $\bar{F}^{tt}_{\rho\rho}$ which varies inversely proportional to the gap.

The figures illustrate the relative strength of $\bar{F}^{rr}_{\rho\rho}$, $\bar{F}^{rr}_{\beta\beta}$, $\bar{F}^{rr}_{zz}$ which agrees with intuitive arguments. For the centrally placed particle, $\bar{F}^{rr}_{\rho\rho} = \bar{F}^{rr}_{\beta\beta}$ which one can

see in Fig.5.3. However, as particle approaches to the periphery of the cylinder $\bar{F}^{rr}_{\beta\beta}$ increases more than $\bar{F}^{rr}_{\rho\rho}$. The explanation is simple — the velocity gradient due to the relative velocity between the sphere and the cylinder surfaces when rotation is in the azimuthal direction is overall more than that for the radial rotation. Consequently, the azimuthal rotation induces relatively more viscous interactions and more resistance compared to rotation in the radial direction. On the other hand, the gradients in velocity field due to the relative velocity between the particle and conduit surfaces are comparable for both axial and azimuthal rotations. Accordingly, we find that both $\bar{F}^{rr}_{\beta\beta}$ and $\bar{F}^{rr}_{zz}$ have similar values for all $R/(a-a_1)$ and a/a_1.

In Fig.5.4, the normalized nondimensional components of $\mathbf{F}^{rr}$ ($\bar{F}^{rr}_{\rho\rho}$, $\bar{F}^{rr}_{\beta\beta}$, $\bar{F}^{rr}_{zz}$) are plot as functions of the ratio of the radius of the cylinder to the radius of the sphere inside the cylinder a/a_1. In the figures the normalized distance $R/(a-a_1)$ of the center of the sphere from the axis of the cylinder varies as a parameter for different curves. The range of a/a_1 is specifically chosen between 2 to 5 to get results for the intermediate regions where the asymptotic methods can not give results. Fig.5.4 indicates similar conclusions as Fig.5.3.

5.3 Translation-rotation coupling

When the sphere is not in the axisymmetric position, its rotation in certain direction induces hydrodynamic force whereas its translation may generate torque on the suspended body. Symmetry dictates only for radial translation and rotation such couplings are not possible. More specifically, if the particle rotates in the axial or azimuthal directions with its center not on the conduit axis, it encounters force in the azimuthal or axial directions, respectively. Similarly, if the particle translates in the axial or azimuthal directions, it experiences torque in the azimuthal or axial directions, respectively. These couplings between translational and rotational quantities are caused by the presence of the confinement and quantified by the coefficients G

and G' defined in eq.5.3, 5.4.

We non-dimensionalized G and G' with $a_1^2\eta$

$$\bar{G} = \frac{G}{a_1^2\eta} \tag{5.7}$$

$$\bar{G'} = \frac{G'}{a_1^2\eta}, \tag{5.8}$$

and plot $\bar{G}$ and $\bar{G'}$ for different $R/(a-a_1)$ and a/a_1 in Fig.5.5. As expected, for central position with $R = 0$, $\bar{G} = \bar{G'} = 0$ due to axisymmetric configuration. For non-zero R, magnitudes of both coefficients generally increase with decrease in a/a_1 because such variation in relative dimension creates enhanced viscous interactions due to closer proximity between the particle and conduit. However, the behavior of $\bar{G}$ and $\bar{G'}$ with respect to $R/(a-a_1)$ is not monotonous — we can see a reversal in trend and values for both cases. In the subsequent discussion, we intuitively explain this non-monotonic characteristics for both $\bar{G}$ and $\bar{G'}$.

Fig.5.6. is the plot of $\bar{G}$ and $\bar{G'}$ for different $R/(a-a_1)$ and a/a_1 values. Here, a/a_1 varies between 2 and 5 and $R/(a-a_1)$ varies as a parameter for the different curves. The behavior of the normalized non-zero components of $\mathbf{F}^{tr}$ and $\mathbf{F}^{rt}$ are similar to Fig.5.5.

According to eq.5.3 and 5.4, G is the coefficient which relates either axial rotation with azimuthal force or azimuthal translation with axial torque. The behavior of this coupling constant with increasing $R/(a-a_1)$ can be equivalently explained by considering either of these relations. When the particle rotates in the axial direction, two phenomena influence the hydrodynamic interactions. Firstly, in order to maintain consistent volumetric flow in the gap between the surfaces of the sphere and the cylinder, the pressure-field contains an angular variation which creates a net force in azimuthal direction. Secondly, for a peripheral position of the particle inside the

conduit, lubrication stresses due to the relative motion between the adjacent surfaces contributes in azimuthal force. This two effects are mutually contradictory. Similar azimuthal pressure variation and lubrication effect can be observed for translating particles in the azimuthal direction where again both of these factors tend to cancel each other. The relative influence of the first contribution is stronger than that of the second when the sphere is near the cylinder center and far away from the periphery. The relative effect of lubrication fields, however, increases when the particle approaches near the wall. As a result, the trend in the variation of G with increasing R first reverses and the value start to decay with R after reaching an extrema value. Then the value itself changes sign because of very strong lubrication. This reversal in trend is more prominent for smaller a/a_1 because in that case the pressure variation is strong enough to create a noticeable difference.

The other coefficient G' exhibits a similar pattern of variation with increasing R. It couples either axial translation with azimuthal torque or azimuthal rotation with axial force. As in the case of G, here also along with the near-contact lubrication effect, spatial variation in pressure field plays a key role. Only difference is the variation in pressure field is along the axial direction instead of the angular direction. Again like before, these two effects are subtractive to each other, and near the axisymmetric configuration ($R \to 0$) the relative strength of the pressure differential is predominant over the lubrication effect whereas situation reverses for peripheral position ($R \to a - a_1$). As a result, the change in trend after an extrema value and ultimately a reversal in sign of G' can be observed with increasing R.

5.4 Validation by comparing with the analytical results for limiting cases

We compare a few representative results from our simulation with the values obtained by using different perturbation analysis for different limiting cases. We already know that our computation agrees well with physically intuitive arguments. We also

know that the convergence tests with respect to various computational parameters show a high convergence rate for the algorithm. Moreover, there are a couple of other consistency checks from theoretical point of view. Firstly, the integrand in eq.2.18 have singular components which are nonintegrable over the wave number λ, and cancel each other to give an integrable function only if the analytical derivations are correct. Hence, any error in the derivation is ruthlessly exposed by the non-converging integral. Secondly, the matrix L in eq.4.3 should be a positive definite matrix if it is calculated properly. We confirm that our formulation satisfies both of these consistency conditions. All these tests are, however, necessary checks — they are not sufficient to prove absolute accuracy of our solution. For this purpose, we need some quantitative verification of the numerical study by comparing it with some known exact results.

For quantitative validation, we consider the available theoretical results for axial motion of the sphere in limiting configurations. First, we calculate the translational friction in the axial direction according to the lubrication theory for closely fitted sphere in the cylinder [91]. We assume the particle to be in axisymmetric position and compare our simulation with the theoretical values when $a \sim a_1$. Then, we use the reflection method in axisymmetric configuration and test how our computation matches with it for $a \gg a_1$. The comparison is presented in Fig.5.7 where one can see that our results match perfectly with both theoretical curves in respective regimes. The computation agrees very well with [91] when $a \sim a_1$, but then starts to diverge as a increases. The trend is reverse with the reflection method which differs by less than 1% with the simulated values for $a > 5a_1$ and deviates when $a \sim a_1$.

In Fig.5.8, we account for an eccentric position of the sphere with respect to the cylinder where $R = 2a_1$. For such R, one can not expect that the lubrication theory for tightly fitted sphere would give correct results. Hence, for eccentric configuration, we compare our result only with reflection method. Unlike the axisymmetric case,

here we can compute non-zero G along with $F^{tt}_{\rho\rho}$. We present both coefficients for relative study and find reasonable accuracy (within 1%) between our approach and reflection method when $a > 5R$. Two solutions diverge for lower values of a. For G, this difference is more dramatic where the reversal in the magnitude is evident in simulated data as $a \rightarrow (R + a_1)$. This reversal is due to the lubrication effect which can not be captured by reflection method.

Though we only check the simulated values of the axial frictions with existing results, this quantitative comparison is sufficient to give us confidence in correctness of the entire analysis. In our method, the computation of the friction coefficients is interrelated because these are dependent on elements of grand friction matrix L which is constructed by inverting computed grand mobility M. Hence, correct evaluation of one set of coefficients imply correctness of other components of the friction tensors.

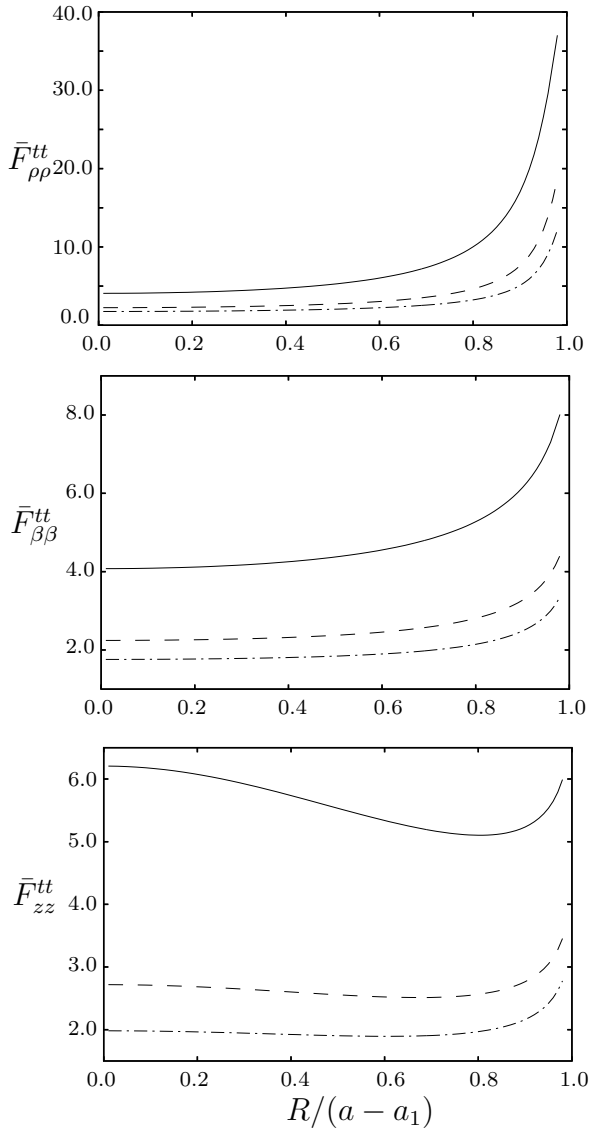

Figure 5.1: Normalized diagonal elements of the translational friction $\mathbf{F}^{tt}$ as functions of non-dimensional position of the sphere center for $a/a_1 = 2$ (solid line), $a/a_1 = 3$ (dashed line), $a/a_1 = 4$ (dash-dot line).

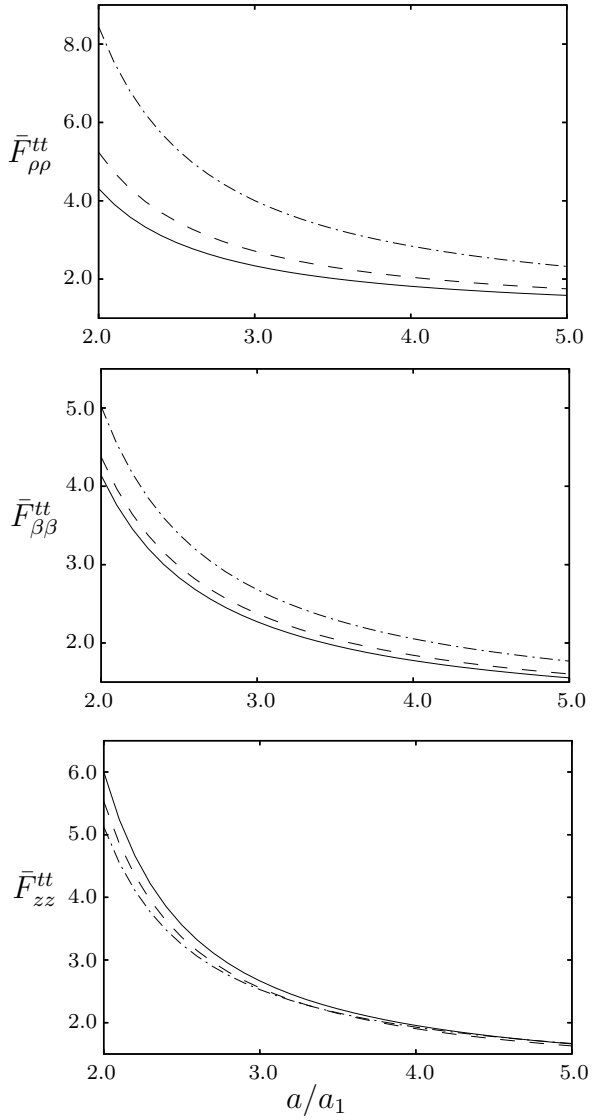

Figure 5.2: Normalized diagonal elements of the translational friction $\mathbf{F}^{tt}$ as functions of a/a_1 for non-dimensional position of the sphere center of $R/(a-a_1) = 0.25$ (solid line), $R/(a-a_1) = 0.5$ (dashed line), $R/(a-a_1) = 0.75$ (dash-dot line).

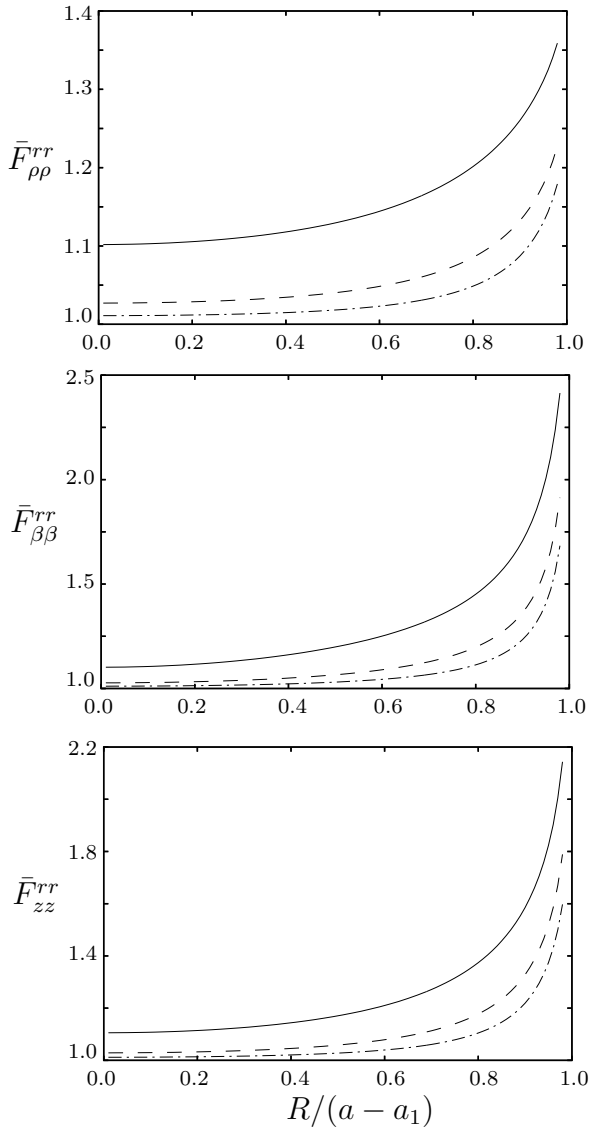

Figure 5.3: Same as Fig.5.1 except normalized diagonal elements of the rotational friction $\mathbf{F}^{rr}$.

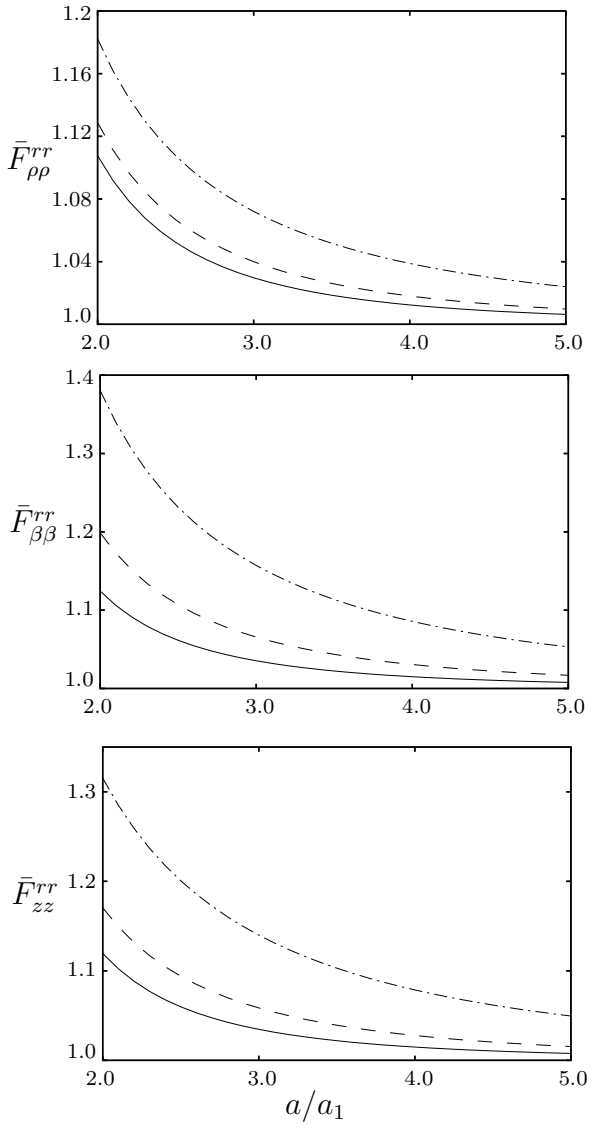

Figure 5.4: Same as Fig.5.2 except normalized diagonal elements of the rotational friction $\mathbf{F}^{rr}$.

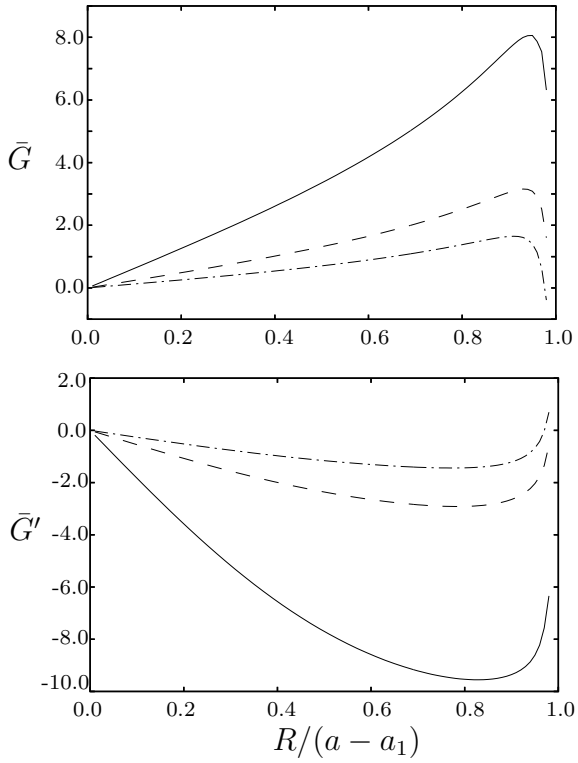

Figure 5.5: Normalized non-zero components of $\mathbf{F}^{tr}$ or $\mathbf{F}^{rt}$ as functions of non-dimensional position of the center of the sphere. Interpretation of the line types are similar to Fig.5.1.

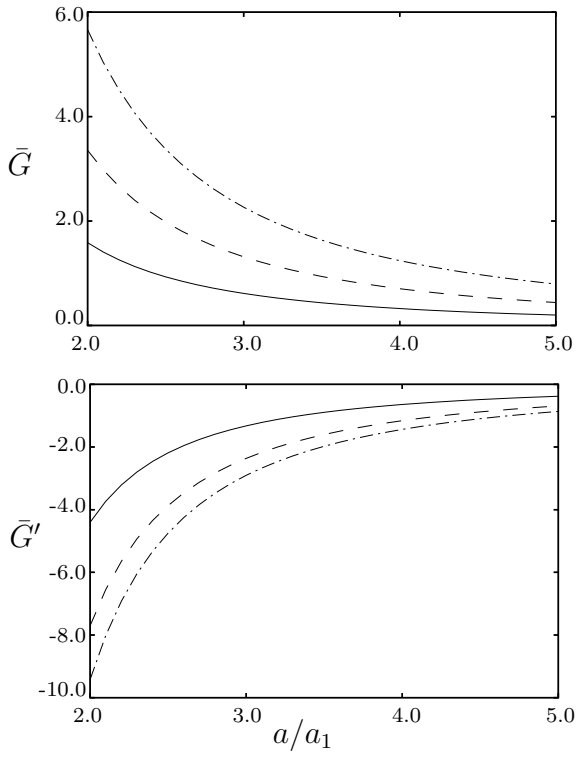

Figure 5.6: Normalized non-zero components of $\mathbf{F}^{tr}$ or $\mathbf{F}^{rt}$ as functions of a/a_1. Interpretation of the line types are similar to Fig.5.2.

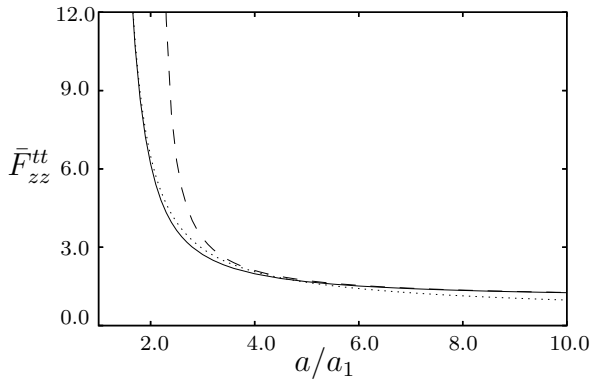

Figure 5.7: Computed values of axial friction for translation (solid line) in axisymmetric configuration are compared with reflection method (dashed line) for $a \gg a_1$ and singular perturbation method (dotted line) for $a \sim a_1$.

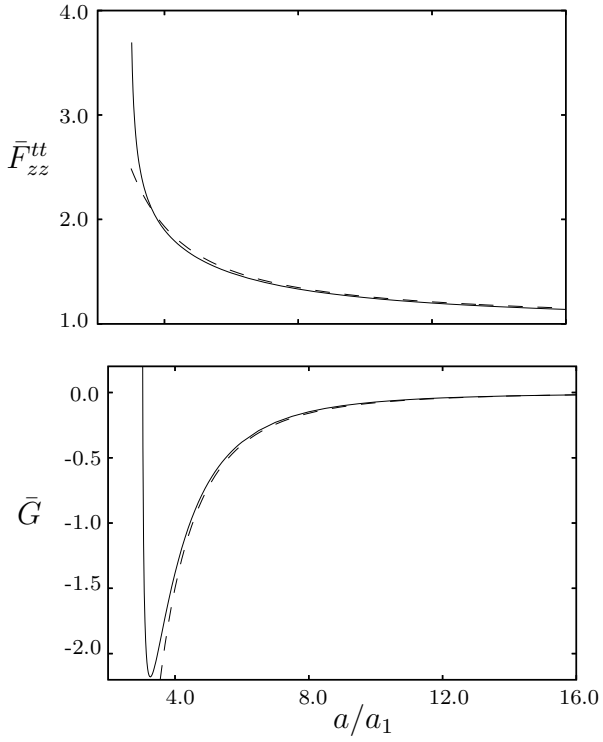

Figure 5.8: Computed values of friction coefficients (solid line) for off-centered position $R = 2a_1$ are compared with reflection method (dashed line) for $a \gg a_1, R$.

CHAPTER 6

PARTICLE-MOTION IN PARABOLIC PRESSURE-DRIVEN FLOW

Our final analysis involves study of particle dynamics in a pressure-driven axial flow for which the variation in velocity profile is parabolic along the radial direction so that the value is maximum at the axis of symmetry and zero at the conduit surface. We address two problems here. First we consider a fixed sphere encountering the impending flow and calculate the force and torque on it. Then we determine the motion of the particle assuming that it is free to move under zero force and zero torque.

6.1 Force and torque on a fixed particle in parabolic velocity field

From symmetry arguments, one concludes that the force $\mathbf{f}^p$ and the torque $\boldsymbol{\tau}^p$ in eqs.4.1 and 4.2 can only have components in the z and β directions, respectively

$$\mathbf{f}^p = f_z^p \hat{\mathbf{e}}_z \tag{6.1}$$

$$\boldsymbol{\tau}^p = \tau_\beta^p \hat{\mathbf{e}}_\beta. \tag{6.2}$$

We normalize f_z^p and τ_β^p

$$\bar{f}_z^p = \frac{f_z^p}{6\pi a_1 \eta u_p} \tag{6.3}$$

$$\bar{\tau}_\beta^p = \frac{\tau_\beta^p}{8\pi a_1^2 \eta u_p}, \tag{6.4}$$

where u_p is the velocity at the cylinder axis due to the parabolic flow. In Fig.6.1, we plot the nondimensional quantities $\bar{f}_z^p$ and $\bar{\tau}_\beta^p$ as functions of $R/(a-a_1)$ for different a/a_1.

In Fig.6.2, we plot the nondimensional quantities $\bar{f}_z^p$ and $\bar{\tau}_\beta^p$ as functions of a/a_1 for different $R/(a-a_1)$. The values of a/a_1 and $R/(a-a_1)$ are chosen similar to that

in Fig.5.2.

The results show that $\bar{f}_z^p$ and $\bar{\tau}_\beta^p$ consistently decrease with increasing a/a_1 because smaller value of a ensures enhanced viscous interactions due to closer proximity between the particle and conduit. For $R = 0$ at the axisymmetric configuration, $\bar{\tau}_\beta^p$ is always zero for any dimension of the cylinder or the sphere. Also, for axisymmetric position of the particle, $\bar{f}_z^p \to 1$ when $a/a_1 \to \infty$. Both of these characteristics can be noticed in Fig.6.1.

As $R/(a - a_1)$ increases, $\bar{f}_z^p$ decreases for any a/a_1. The magnitude of the force on the fixed particle is dependent on the magnitude of the local velocity due to the impending parabolic flow. The impending flow decreases with R due to the parabolic nature. As a result, the force is maximum in the axisymmetric position and decays as the particle approaches towards the cylinder periphery.

The trend of $\bar{\tau}_\beta^p$ with increasing $R/(a-a_1)$ is reverse. The torque is approximately proportional to the local shear rate which is zero at $R = 0$ and increases with R. As a result, when the particle moves away from the axis of the cylinder, $\bar{\tau}_\beta^p$ increases. Fig.6.2. shows similar trends.

6.2 Motion of a free-particle in Poiseuille flow

A free particle is free of inertia and external force so that net viscous force and torque on it are zero. Hence, the motion of such particle can be determined by fixing $\mathbf{f}^{ex} = \mathbf{f} = \mathbf{0}$ and $\boldsymbol{\tau} = \boldsymbol{\tau}^{ex} = \mathbf{0}$. Accordingly, we solve eqs.4.1 and 4.2 simultaneously to find $\mathbf{u}$ and $\boldsymbol{\omega}$. Symmetry dictates

$$\mathbf{u} = u_z \hat{\mathbf{e}}_z \tag{6.5}$$

$$\boldsymbol{\omega} = \omega_\beta \hat{\mathbf{e}}_\beta. \tag{6.6}$$

In Fig.6.3, we present normalized u_z and ω_β as functions of $R/(a-a_1)$ for different a/a_1. Similarly, in Fig.6.4. the values of a/a_1 are varied and $R/(a-a_1)$ is treated as a parameter for the different curves. This result shows the trend of normalized u_z and ω_β as both a/a_1 and $R/(a-a_1)$ varies.

For large values of a/a_1, a free particle follows the fluid with a speed similar to the local velocity of the impending field. As a result, it can be treated as a tracer particle, and the u_z vs R curve represents the parabolic velocity profile across the channel. We can observe this in Fig.6.3. When the sphere is near the surface of the cylinder, the curves depart from the parabolic function due to the effect of the reflected flow from the confinement. This departure is especially pronounced for narrow cylinders.

The rotational velocity of the sphere is proportional to the local shear of the impending flow. This is why $\omega_\beta = 0$ at $R = 0$ because the shear is zero on the axis of the cylinder. The angular velocity increases linearly with R following the behavior of the local shear for different radial positions. This characteristics is consistently manifested in Fig.6.3. Exception happens only when the particle is very close to the wall. Then the angular velocity starts to decay with R because of the lubrication effect.

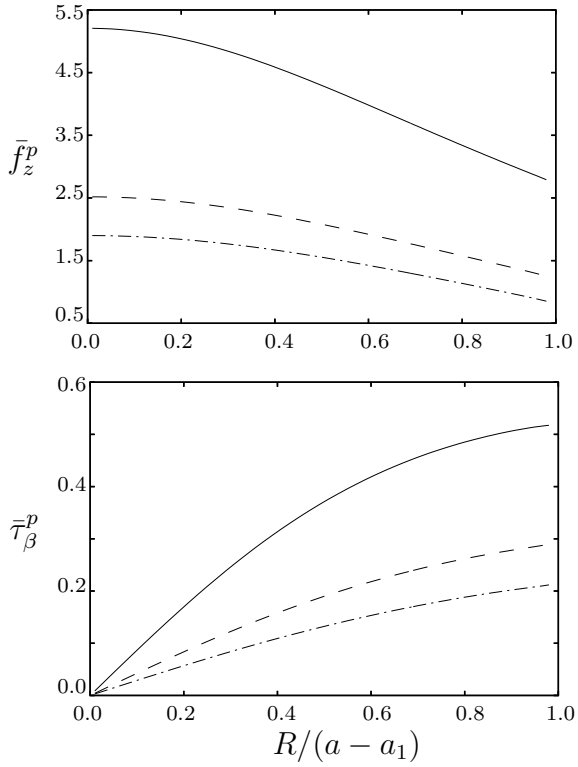

Figure 6.1: Normalized force and torque on a fixed sphere in pressure-driven parabolic flow as functions of its normalized radial position. The interpretation of the line types are similar to Fig.5.1.

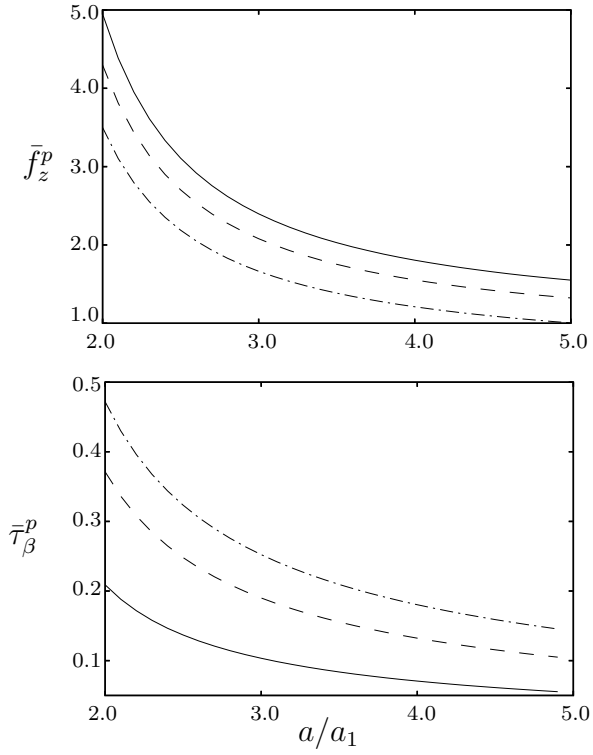

Figure 6.2: Normalized force and torque on a fixed sphere in pressure-driven parabolic flow as functions of the ratio of cylinder radius to the sphere radius a/a_1. The interpretation of the line types are similar to Fig.5.2.

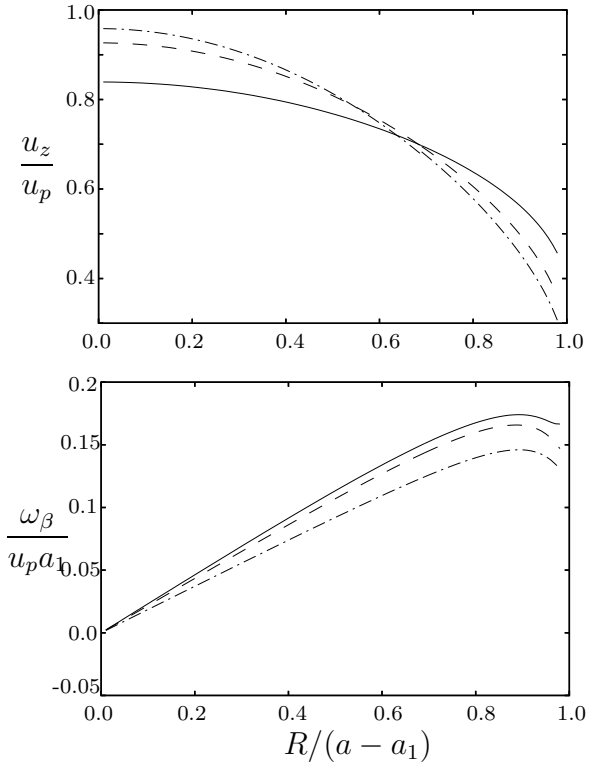

Figure 6.3: The linear and angular velocities of a free particle in pressure-driven parabolic flow as functions of its normalized radial position. The interpretation of the line types are similar to Fig.5.1.

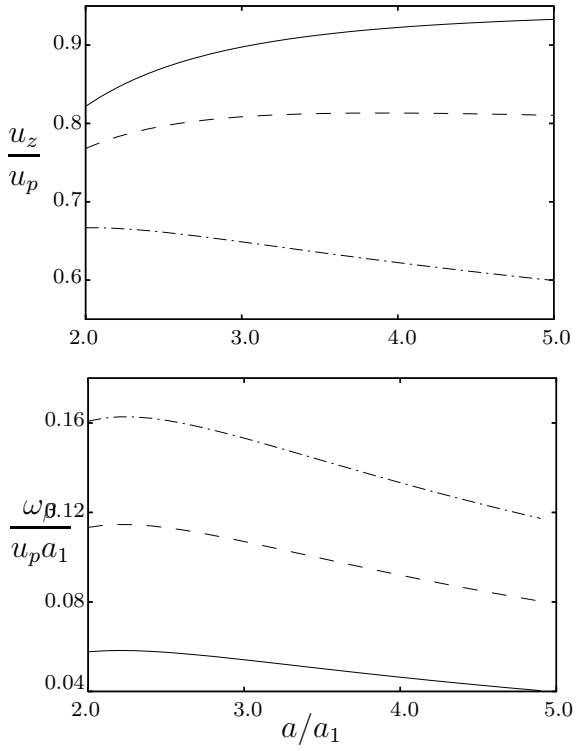

Figure 6.4: The linear and angular velocities of a free particle in pressure-driven parabolic flow as functions of the ratio of cylinder radius to the sphere radius a/a_1. The interpretation of the line types are similar to Fig.5.2.

CHAPTER 7

SUMMARY AND CONCLUDING REMARKS

In this thesis, we outline a general mathematical procedure (basis transformation method) which can be used to develop fast algorithm to address fluid-mechanical problems involving suspended particles inside conduits. The method enables us to construct general reflection relations to satisfy vector boundary conditions at disconnected simple surfaces. We specifically concentrate on solving Stokesian dynamics of a sphere in a cylinder. Unlike past analytical studies, the proposed method is applicable for all possible particle-conduit configurations, i.e. we can consider any dimensions and particle-position to define the system. The generality of our approach also allows us to describe not only the axial motion of the particle but also all possible translations and rotations including those in the radial and azimuthal directions. To our knowledge, our results are first such comprehensive study of general motion of a spherical particle inside a cylindrical vessel.

The numerical scheme is extremely efficient because of the high convergence rates. According to our experience, we can obtain reasonable results within 1% accuracy using less than a minute computational time in a 2GHz machine.

We present a few representative results for different relative dimensions of the sphere and the cylinder as well as for different radial positions of the particle. We especially choose the configurations where all three defining dimensions are comparable to each other because available asymptotic methods are not applicable in those cases. We consider the particle to be either undergoing specified motion in quiescent fluid or encountering an impending pressure-driven parabolic flow. By definition, the first problem is a friction problem where the hydrodynamic force and torque on the sphere are evaluated for prescribed motion in stagnant fluid. For the second situation, however, one can furnish both friction and mobility descriptions. Accordingly,

we evaluate force and torque on a fixed particle in a parabolic flow (friction formulation) as well as determine the motion of a force-free torque-free particle in the same impending field (mobility formulation). The simulation results coincide properly with intuitive physical arguments.

We validate our simulation data in several ways. First of all, the convergence tests can be treated as necessary verification which, though can not quantify absolute accuracy, at least can check consistency. Then there are two independent validations from theoretical point of view. Integrability of the integrand in eq.2.18 can only be ensured if the analytical derivations are correct. Secondly, the matrix L in eq.4.3 should be positive definite which we confirm. Apart from these tests, we also compare our results with different asymptotic methods for limiting cases. The agreements between the two sets of results are satisfactory.

Though the primary focus of this article is on solving Stokesian fields around a sphere inside a cylinder where the velocity is specified at the solid-fluid interfaces, the outlined basis transformation method has a far more general applicability. As this method does not require symmetry constraints like recently proposed Cartesian representation method [77, 111], the presented formulation can be used in various situations. Hence, it can be applied to solve different second order vector differential equation with linear boundary conditions specified at different disconnected simple surfaces. Only restriction on the governing equation and geometries is that the basis solutions of the linear differential equation for the involved coordinate systems have to be in separable form as given in eqs.2.1 and 2.2. Fortunately, in a wide range of fluid-mechanical problems, the separable basis solutions can be constructed.

In the future, we can explore all these possibilities. Firstly, we can extend this method to multi-particle systems in cylindrical conduit. Furthermore, simple modifications of the reflection relations would allow us to consider many body interactions in annular geometries. Finally, we can also apply basis transformation method to vector equations other than steady Stokes equation and to boundary conditions other

than Dirichlet conditions. As a result, the problems involving periodically oscillating fields (unsteady Stokes equation) or stress-free interfaces (Neumann condition) or surfactant covered surfaces (mixed boundary conditions) can also be addressed.

BIBLIOGRAPHY

[1] P. K. Shin, P. Pawar, K. Konstantopoulos, and J. M. Ross. Characteristics of new Staphylococcus aureus-RBC adhesion mechanism independent of fibrinogen and IgG under hydrodynamic shear conditions. *Am. J. Physiol. Cell Physiol.*, 289:C727–C734, 2005.

[2] PH. Lavalle, J. F. Stoltz, B. Senger, J. C. Voegel, and P. Schaaf. Red blood cell adhesion on a solid/ liquid interface. *Proc. Natl. Acad. Sci. USA*, 93:15136–15140, 1996.

[3] J. K. Armstrong, R. B. Wenby, H. J. Meiselman, and T. C. Fisher. The hydrodynamic radii of macromolecules and their effect on red blood cell aggregation . *Biophys. J.*, 87:4259–4270, 2004.

[4] T. K. Hsiai, S. K. Cho, P. K. Wong, M. H. Ing, A. Salazar, S. Hama, M. Navab, L. L. Demer, and H. Chih-Ming. Micro sensors: linking real-time oscillatory shear stress with vascular inflammatory responses. *Annals of Biomedical Eng.*, 32:189–201, 2004.

[5] M. Abkarian, M. Faivre, and H. A. Stone. High speed microfluidic differential manometer for cellular-scale hydrodynamics. *PNAS*, 103:538–542, 2006.

[6] J. A. Davis, D. W. Inglis, K. J. Morton, D. A. Lawrence, L. R. Huang, S. Y. Chou, J. C. Sturm, and R. H. Austin. Deterministic hydrodynamics: Taking blood apart. *PNAS*, 103:14779–14784, 2006.

[7] O. Brandt. Interaction of blood-cells/-components and tissue cells with body foreign surfaces in a cone plate rheometer under hydrodynamic shear load. *Clin. Hemorh. and Microcirc.*, 32:145–149, 2005.

[8] M. Rocco, B. Spotorno, and R. R. Hantgan. Modeling the alpha(IIb)beta(3)integrin solution conformation. *Protein Sci.*, 2:2154–2166, 1993.

[9] T. H. Fan and A. G. Fedorov. Analysis of hydrodynamic interactions during AFM imaging of biomedical membranes. *Langmuir*, 19:1347–1356, 2003.

[10] D. C. Prieve, F. Luo, and F. Lanni. Brownian-motion of a hydrosol particle in a colloidal force-field. *Faraday Discuss. Chem. Soc.*, 83:297, 1987.

[11] J. Y. Walz and L. Suresh. Study of the sedimentation of a single particle toward a flat plate. *J. Chem. Phys.*, 103:10714–725, 1995.

[12] D. L. Sober and J. Y. Walz. Measurement of long-range depletion energies between a colloidal particle and a flat surface in micellar solutions. *Langmuir*, 11:2352, 1995.

[13] M. Frank, D. Anderson, E. R. Weeks, and J. F. Morris. Particle migration in pressure-driven flow of a Brownian suspension. *J. Fluid Mech.*, 493:363–78, 2003.

[14] W. J. Weiss. Pulsatile pediatric ventricular assist devices. *ASAIO J.*, 51:540–545, 2005.

[15] X. R. Zhu, M. Y. Zhang, G. G. Zhang, and H. N. Liu. Numerical investigation on hydrodynamics and biocompatibility of a magnetically suspended axial blood pump. *ASAIO J.*, 52:624–629, 2006.

[16] J. T. Zhang, B. Gellman, A. Koert, K. A. Dasse, R. J. Gilbert, B. P. Griffith, and Z. J. J. Wu. Computational and experimental evaluation of the fluid dynamics and hemocompatibility of the CentriMag blood pump. *Artificial Organs*, 30:168–177, 2006.

[17] K. Kido, H. Hoshi, N. Watanabe, H. Kataoka, K. Ohuchi, J. Asama, T. Shinshi, M. Yoshikawa, and S. Takatani. Computational fluid dynamics analysis of the pediatric tiny centrifugal blood pump(TinyPump). *Artificial Organs*, 30:392–399, 2006.

[18] T. W. Secomb, R. Hsu, and A. R. Pries. Motion of red blood cells in a capillary with an endothelial surface layer: effect of flow velocity. *Am. J. Physiol. Heart Circ. Physiol.*, 281:H629–H636, 2001.

[19] R. H. Zhou, J. Gordon, A. F. Palmer, and H. C. Chang. Role of erythrocyte deformability during capillary wetting. *Biotech. and Bioeng.*, 93:201–211, 2006.

[20] W. S. J. Uijttewaal, E. J. Nijhof, P. J. H. Bronkhorst, E. Denhartog, and R. M. Heethaar. Near-wall excess of platelets induced by lateral migration of erythrocytes in flowing blood. *Am. J. Physiol.*, 264:H1239–H1244, 1993.

[21] H. Shankaran, P. Alexandridis, and S. Neelamegham. Aspects of hydrodynamic shear regulating shear-induces platelet activation and self-association of von Willebrand factor in suspension. *Blood*, 101:2637–2645, 2003.

[22] O. J. T. McCarty, S. Jadhav, M. M. Burdick, W. R. Bell, and K. Konstantopoulos. Fluid shear regulates the kinetics and molecular mechanisms of activation-dependent platelet binding to colon carcinoma cells . *Biophys. J.*, 83:836–848, 2002.

[23] P. Pawar, P. K. Shin, S. A. Mousa, J. M. Ross, and K. Konstantopoulos. Fluid shear regulates the kinetics and receptor specificity of Staphylococcus aureus binding to activated platelets. *J. Immunology*, 173:1258–1265, 2004.

[24] Z. M. Ruggeri, J. N. Orje, R. Habermann, A. B. Federici, and A. J. Reininger.

Activation-independent platelet adhesion and aggregationunder elevated shear. *Blood*, 108:1903–1910, 2006.

[25] N. B. Purvis and T. D. Giorgio. The effects of elongational stress exposure on the activation and aggregation of blood-platelets. *Biorheology*, 28:355–367, 1991.

[26] A. J. Reininger, H. F. G. Heijnen, H. Schumann, H. M. Specht, H. Schramm, and Z. M. Ruggeri. Mechanism of platelet adhesion to von Willebrand factor and microparticle formation under high shear stress. *Blood*, 107:3537–3545, 2006.

[27] J. N. Zhang, A. L. Bergeron, Q. H. Yu, C. Sun, L. McBride, P. F. Bray, and J. F. Dong. Duration of exposure to high fluid shear stress is critical in shear-induced platelet activation-aggregation. *Thrombosis and Haemostasis*, 90:672–678, 2003.

[28] P. Y. Huang and J. D. Hellums. Aggregation and disaggregation kinetics of human blood platelets .3. the disaggregation under shear-stress of platelet aggregates. *Biophys. J.*, 65:354–361, 1993.

[29] S. Neelamegham, A. D. Taylor, H. Shankaran, C. W. Smith, and S. I. Simon. Shear and time-dependent changes in Mac-1, LFA-1, and ICAM-3 binding regulate neutrophil homotypic adhesion. *J. Immunology*, 164:3798–3805, 2000.

[30] J. A. DiVietro, M. J. Smith, B. R. E. Smith, L. Petruzzelli, R. S. Larson, and M. B. Lawrence. Immobilized IL-8 triggers progressive activation of neotrophils rolling in vitro on P-Selectin and intercellular adhesion molecule-1. *J. Immunology*, 167:4017–4025, 2001.

[31] S. Neelamegham, A. D. Taylor, Burns A. R., C. W. Smith, and S. I. Simon.

Hydrodynamic shear shows distinct roles for LFA-1 and Mac-1 in neutrophil adhesion to intercellular adhesion molecule-1. *Blood*, 92:1626–1638, 1998.

[32] P. Tandon and S. L. Diamond. Kinetics of beta2-integrin and L-selection bonding during neutrophil aggregation in shear flow. *Biophys. J.*, 75:3163–3178, 1998.

[33] S. Neelamegham, A. D. Taylor, Hellums J. D., M. Dembo, C. W. Smith, and S. I. Simon. Modelling the reversible kinetics of neutrophil aggregation under hydrodynamic shear. *Biophys. J.*, 72:1527–1540, 1997.

[34] T. K. Hsiai, S. K. Cho, Wong P. K., M. Ing, A. Salazar, A. Sevanian, M. Navab, L. L. Demer, and Ho C. M. Monocyte recruitment to endothelial cells in reponse to oscillatory shear stress. *FASEB J.*, 17:1648–1657, 2003.

[35] A. Karsan, C. J. Cornrjo, R. K. Winn, B. R. Schwartz, W. Way, N. Lannir, R. Gershoni-Beruch, A. Etzioni, H. D. Ochs, and J. M. Harlan. Leukocyte adhesion deficiency type II is a generalized defect of De Novo GDP-Fucose biosynthesis . *J. Clin. Invest.*, 101:2438–2445, 1998.

[36] M. R. King, M. B. Kim, I. H. Sarelius, and D. A. Hammer. Hydrodynamic interactions between rolling leukocytes In Vivo. *Microcirculation*, 10:401–409, 2003.

[37] M. R. King and D. A. Hammer. Multiparticle adhesive dynamics:hydrodynamic recruitment of rolling leukocytes. *PNAS*, 98:14919–14924, 2001.

[38] H. P. Xu, A. Manivannan, K. A. Goatman, H. R. Jiang, J. Liversidge, P. F. Sharp, J. V. Forrseter, and I. J. Crane. Reduction in shear stress activation of the endothelium, and leukocyte priming are all recquired for leukocyte passage across the blood-retina barrier. *J. Leukocyte Biology*, 75:224–232, 2004.

[39] S. I. Simon and H. L. Goldsmith. Leukocyte adhesion dynamics in shear flow. *Annals of Biomed. Eng.*, 30:315–332, 2002.

[40] M. B. Lawrence, G. S. Kansas, E. J. Kunkel, and K. Ley. Thereshold levels of fluid shear promote leukocyte adhesion through selectins(CD62L,P,E). *J. Cell Biology*, 136:717–727, 1997.

[41] R. Dillon, L. Fauci, and D. Gaver. A microscale model of bacterial swimming, chemotaxis and substrate transport. *J. theor. Biol.*, 177:325–340, 1995.

[42] M. U. Nollert, S. L. Diamond, and L. V. Mcintire. Hydrodynamic shear-stress and mass-transport modulation of endothelial-cell metabolism. *Biotech. and Bioeng.*, 38:588–602, 1991.

[43] A. Prokop and R. K. Bajpai. The sensitivity of biocatalysts to hydrodynamic shear-stress. *Adv. App. Microbiol.*, 37:165–232, 1992.

[44] J.C. Liao, T. W. Hein, M.W. Vaughn, K.T. Huang, and L. Kuo. Intravascular flow decreases erythrocyte consumption of nitric oxide. *PNAS*, 96:8757–8761, 1999.

[45] M. J. Moehlenbrock, A. K. Price, and R. S. Martin. Use of microchip-based hydrodynamic focusing to measure the deformation-induced release of ATP from erythrocytes. *Analyst*, 131:930–937, 2006.

[46] A. S. Drochon and R. Chotard-Ghodsnia. Blood and circulating cells: from rheology to clinical challenges. *Houille Blanche-Revue Internationale de l Eau*, 4:56–59, 2005.

[47] C. Dong, R. S. Chadwick, and A. N. Schechter. Influence of sickle hemoglobin polymerization and membrane-properties on deformability of sickle erythrocytes in the microcirculation. *Biosphys. J.*, 63:774–783, 1992.

[48] L. G. Cima, D. E. Discher, and M. C. Tong, J. Williams. A hydrodynamic imterpretation of crisis in sickle-cell-anemia. *Microvascular Research*, 47:41–54, 1994.

[49] R. Haier, T. Korb, B. Hotz, H. U. Spiegel, and N. Senninger. An intravital model to monitor steps of metastasis tumor cell adhesion within the hepatic microcirculation. *J. Gastrointestinal Surgery*, 7:507–514, 2003.

[50] A. von Sengbusch, P. Gassmann, K. M. Fisch, A. Enns, G. L. Nicolson, and J. Haier. Focal adhesion kinase regulates metastatic adhesion of carcinoma cells within liver sinusoids. *Am. J. Pathol*, 166:585–596, 2005.

[51] J. Haier and G. L. Nicolson. The role of tumor cell adhesion as an important factor in formation of distant colorectal metastasis. *Diseases of the Colon and Rectum*, 44:876–884, 2001.

[52] D. S. Lee, H. Rieger, and K. Bartha. Flow correlated percolation during vascular remodeling in growing tumor. *Phys. Rev. Lett.*, 96, 2006.

[53] S. M. Razavian, M. Delpino, A. Simon, and J. Levenson. Increase in erythrocyte disaggregation shear-stress in hypertension . *Hypertension*, 20:247–252, 1992.

[54] Y. V. Rumyantseva, N. S. Smetanina, N. N. Firsov, S. A. Plyasunova, O. A. Schurova, E. G. Lukyanova, L. Y. Fetisova, and O. M. Yakunina. Kinetics of spontaneous aggregation and shear disaggregation of erythrocytes in thalassemia patients. *Gematologiya I Transfuziologiya*, 47:19–22, 2002.

[55] G.K. Youngren and A. Acrivos. Stokes flow past a particle of arbitary shape: a numerical method of solution. *J. Fluid Mech.*, 69:377–403, 1975.

[56] S. Kim and S. J. Karrila. *Microhydrodynamics: Principles and Selected Applications*. Butterworth-Heinemann, London, 1991.

[57] P. Ganatos, S. Weinbaum, and R. Pfeffer. A strong interaction theory for the creeping motion of a sphere between plane parallel boundaries. Part 1. Perpendicular motion. *J. Fluid Mech.*, 99:739–53, 1980.

[58] P. Ganatos, R. Pfeffer, and S. Weinbaum. A strong interaction theory for the creeping motion of a sphere between plane parallel boundaries. Part 2. Parallel motion. *J. Fluid Mech.*, 99:755–83, 1980.

[59] A. Z. Zinchenko and R. H. Davis. Large-scale simulations of concentrated emulsion flows. *Phil. Trans. R. Soc. Lond. A*, 361:813–45, 2003.

[60] M. E. Staben, A. Z. Zinchenko, and R. H. Davis. Motion of a particle between two parallel plane walls in low-Reynolds-number Poiseuille flow. *Phys. Fluids.*, 15:1711–33, 2003.

[61] C. Pozrikidis. Interfacial dynamics for Stokes flow. *J. Comput. Phys.*, 169:250–301, 2001.

[62] C. Pozrikidis. Numerical simulation of cell motion in tube flow. *Annals of Biomed. Eng.*, 33:165–178, 2005.

[63] M. Vergeles, P. Keblinski, J. Koplik, and J. R. Banavar. Stokes drag and lubrication flows: A molecular dynamics study. *Phys. Rev. E*, 53:4852–64, 1996.

[64] C. Trozzi and G. Ciccotti. Stationary nonequilibrium states by molecular dynamics. II. Newton's law. *Phys. Rev. A*, 29:916–925, 1984.

[65] I. Bitanis, S.A. Somers, H.T. Davis, and M. Tirrell. Microscopic dynamics of flow in molecularly narrow pores. *J. Chem. Phys.*, 93:3427–3431, 1990.

[66] J. Koplik, J.R. Banavar, and J.F. Willemsen. Molecular dynamics of fluid flow at solid surfaces. *Phys. Fluids A*, 1:781–794, 1989.

[67] M. Vergeles, P. Keblinski, J. Koplik, and J. R. Banavar. Stokes drag at the molecular level. *Phys. Rev. Lett.*, 75:232–5, 1995.

[68] P.A. Thompson and M.O. Robbins. Shear flow near solids: Epitaxial order and flow boundary conditions. *Phys. Rev. A*, 41:6830–6837, 1990.

[69] P.A. Thompson, G.S. Grest, and M.O. Robbins. Phase transitions and universal dynamics in confined films. *Phys. Rev. Lett.*, 68:3448–3451, 1992.

[70] W. Loose and G. Ciccotti. Temperature and temperature control in nonequilibrium-molecular-dynamics simulations of the shear flow of dense liquids. *Phys. Rev. A*, 45:3859–3866, 1992.

[71] B. Cichocki, B. U. Felderhof, K. Hinsen, E. Wajnryb, and J. Bławzdziewicz. Friction and mobility of many spheres in Stokes flow. *J. Chem. Phys.*, 100:3780–3790, 1994.

[72] A. S. Sangani and G. B. Mo. An $O(N)$ algorithm for Stokes and Laplace interactions of particles. *Phys. Fluids*, 8:1990–2010, 1996.

[73] A. V. Filippov. Drag torque on clusters of N arbitrary spheres at low Reynolds number. *J. Colloid Interface Sci.*, 229:184–95, 2000.

[74] B. Cichocki, M. L. Ekiel-Jeżewska, G. Nagele, and E. Wajnryb. Motion of spheres along fluid–gas interface. *J. Chem. Phys.*, 121:2305–16, 2004.

[75] B. Cichocki, M. L. Ekiel-Jeżewska, and E. Wajnryb. Hydrodynamic interactions between spheres in a viscous fluid with a flat free surface or hard wall. *J. Chem. Phys.*, pages 1–3, 2007.

[76] R. B. Jones. Spherical particle in Poiseuille flow between planar walls. *J. Chem. Phys.*, 121:483–500, 2004.

[77] S. Bhattacharya, J. Bławzdziewicz, and E. Wajnryb. Hydrodynamic interactions of spherical particles in suspensions confined between two planar walls. *J. Fluid Mech.*, 541:263–292, 2005.

[78] S. Bhattacharya, J. Bławzdziewicz, and E. Wajnryb. Hydrodynamic interactions of spherical particles in Poiseuille flow between two parallel walls. *Phys. Fluids*, 18(5), 2006.

[79] S. Bhattacharya, J. Bławzdziewicz, and E. Wajnryb. Far-field approximation for hydrodynamic interactions in parallel-wall geometry. *J. Comput. Phys.*, 212:718–738, 2006.

[80] R.G. Cox and S.G.. Mason. Suspended particles in fluid flow through tubes. *Annu. Rev. Fluid Mech.*, 3:291–316, 1971.

[81] J. Brenner, H.and Happel. Slow viscous flow past a sphere in a cylindrical tube. *J. Fluid Mech.*, 4:195–213, 1958.

[82] R. G. Cox and H. Brenner. Effect of finite boundaries on Stokes resistance of an arbitrary particle. 3. Translation and rotation. *J. Fluid Mech.*, 28:391, 1967.

[83] T. Greenstein and J. Happel. Theoretical study of the slow motion of a sphere and a fluid in a cylindrical tube. *J. Fluid Mech.*, 34:705–710, 1968.

[84] H. Brenner. Pressure drop due to the motion of neutrally buoyant particles in duct flows. *J. Fluid Mech.*, 43:641–660, 1970.

[85] T. Greenstein and J. Happel. Viscosity of dilute uniform suspensions of sphere spheres. *Phys. Fluids*, 13:18–21, 1970.

[86] H. Tozeren. Torque on eccentric spheres flowing in tubes. *J Applied Mechanics-Transactions of the ASME*, 49:279–283, 1982.

[87] H. Tozeren. Drag on eccentrically positioned spheres translating and rotating in tubes. *J. Fluid Mech.*, 129:77–90, 1983.

[88] A.J. Goldman, R.G. Cox, and H. Brenner. Slow viscous motion of a sphere parallel to a plane wall-I. Motion through a quiscent fluid. *Chem. Engng. Sci.*, 22:637–651, 1967.

[89] M. E. O'Neill and K. Stewartson. On the slow motion of a sphere parallel to a nearby plane wall. *J. Fluid Mech.*, 27:705–724, 1967.

[90] A. Falade and H. Brenner. Stokes wall effects for particles moving near cylindrical boundaries. *J. Fluid Mech.*, 154:145–162, 1985.

[91] P.M. Bungay and H. Brenner. The motion of a closely-fitting sphere in a fluid-filled tube. *Int. J. Multiphase Flow*, 1:25–56, 1973.

[92] P.M. Bungay and H. Brenner. Pressure drop due to the motion of a sphere near the wall bounding a Poisseuille flow. *J. Fluid Mech.*, 60:81–96, 1973.

[93] C. Pozrikidis. Computation of Stokes flow due to the motion or presence of a particle in a tube. *Journal of Engineering Mathematics*, 53:1–20, 2005.

[94] C. Queguiner and D. BarthesBiesel. Axisymmetric motion of capsules through cylindrical channels. *J. Fluid Mech.*, 348:349–376, 1997.

[95] J. J. L. Higdon and G. P. Muldowney. Resistance functions for spherical particles, droplets and bubbles in cylindrical tubes. *J. Fluid Mech.*, 298:193–210, 1995.

[96] W.J. Lunsmann, L. Genieser, R.C. Armstrong, and R.A. Brown. Finite-element analysis of steady viscoelastic flow around a sphere in a tube-Calculations with constant viscosity models. *Journal of Non-Newtonian Fluid Mechanics*, 48:63–99, 1993.

[97] M. SugiharaSeki. The motion of an ellipsoid in tube flow at low Reynolds numbers. *J. Fluid Mech.*, 324:287–308, 1996.

[98] R. SugiharaSeki, M.and Skalak. Asymmetric flows of spherical particles in a cylindrical tube. *Biorheology*, 34:155–169, 1997.

[99] N. Sushko and M. Cieplak. Motion of grains, droplets, and bubbles in fluid-filled nanopores. *Physical Review E*, 64, 2001.

[100] G. Drazer, B. Khusid, Koplik, J., and A. Acrivos. Wetting and particle adsorption in nanoflows. *Phys. Fluids*, 17, 2005.

[101] L. Durlofsky, J. F. Brady, and G. Bossis. Dynamic simulation of hydrodynamically interacting particles. *J. Fluid Mech.*, 180:21–49, 1987.

[102] A. J. C. Ladd. Hydrodynamic interactions in suspensions of spherical particles. *J. Chem. Phys.*, 88:5051, 1988.

[103] B. U. Felderhof and R. B. Jones. Displacement theorems for spherical solutions of the linear Navier-Stokes equations. *J. Math. Phys.*, 30:339–42, 1989.

[104] A. Sierou and J. F. Brady. Accelerated Stokesian dynamics simulations. *J. Fluid Mech.*, 448:115–46, 2001.

[105] L. J. Durlofsky and J. F. Brady. Dynamic simulation of bounded suspensions of hydrodynamically interacting particles. *J. Fluid. Mech.*, 200:39–67, 1989.

[106] P.R. Nott and J.F. Brady. Pressure-driven flow of suspensions—simulation and theory. *J. Fluid Mech.*, 275:157–199, 1994.

[107] J. F. Morris and J. F. Brady. Pressure-driven flow of a suspension: Buoyancy effects. *Int. J. Multiphase Flow*, 24:105–30, 1998.

[108] B. Cichocki and R. B. Jones. Image representation of a spherical particle near a hard wall. *Physica A*, 258:273–302, 1998.

[109] B. Cichocki, R. B. Jones, R. Kutteh, and E. Wajnryb. Friction and mobility for colloidal spheres in Stokes flow near a boundary: The multipole method and applications. *J. Chem. Phys.*, 112:2548–61, 2000.

[110] S. Bhattacharya and J. Bławzdziewicz. Image system for Stokes-flow singularity between two parallel planar walls. *J. Math. Phys.*, 43:5720–31, 2002.

[111] S. Bhattacharya, J. Bławzdziewicz, and E. Wajnryb. Many-particle hydrodynamic interactions in parallel-wall geometry: Cartesian-representation method. *Physica A*, 356:294–340, 2005.

[112] H. Lamb. *Hydrodynamics.* Dover, New York, 1945.

APPENDIX A

DERIVATION OF THE TRANSFORMATION COEFFICIENTS

In this appendix, we derive the expressions of transformation coefficients $T_r(\mathbf{R}|lm0,\lambda\mu2)$, $T_r(\mathbf{R}|lm1,\lambda\mu2)$, $T_r(\mathbf{R}|lm2,\lambda\mu2)$ given in eqs.3.48—3.52. According to our analysis, if these constants are known, we can find all other elements in T_r and T_f by using eqs.3.12, 3.13, 3.14, 3.15, 3.34.

A.1 Transformation relation between two sets of scalar harmonics

Because of our choice $q^+ = q_1^+$ (both are i), eq.3.14 ensures

$$T_r(\mathbf{R}|lm2|\lambda\mu2) = T_r(\mathbf{R}|lm0|\lambda\mu0). \tag{A.1}$$

Then, according to eq.3.15, one can write

$$\mathbf{v}^+_{\lambda\mu0} = \sum_{lm} \mathbf{v}^{1+}_{lm0}\, T_r(\mathbf{R}|lm0,\lambda\mu0) = \sum_{lm} \mathbf{v}^{1+}_{lm0}\, T_r(\mathbf{R}|lm2,\lambda\mu2) \tag{A.2}$$

which implies that the potential solution of Stokes equation can not have any coupling with vorticity and pressure solutions. Considering eq.3.16—3.19, we conclude

$$\Phi^+_{\lambda\mu} = \sum_{lm} \Phi^{1+}_{lm}\; T_r(\mathbf{R}|lm0,\lambda\mu0) \tag{A.3}$$

In our analysis, $T_r(\mathbf{R}|lm2|\lambda\mu2)$ is obtained by relating the scalar harmonic functions $\Phi^+_{\lambda\mu}$ and Φ^{1+}_{lm} defined in eq.3.20—3.23.

By using properties of the modified Bessel function $I_\mu(\lambda\rho)$, $\Phi^+_{\lambda\mu}$ can be expanded

$$\Phi^+_{\lambda\mu} = \frac{1}{4\pi^2}\int_0^{2\pi} \exp[\lambda\rho\cos(\beta-\psi) + i\mu\psi + i\lambda z]\; d\psi. \tag{A.4}$$

If cylinder center and sphere center is separated by $\mathbf{R} = R\hat{\mathbf{e}}_x$, then from geometry